Master of Science Thesis

Numerical Study of Fluid Structure Interaction in Nuclear Reactor Applications

Eline ter Hofstede

August 20, 2015

Aerodynamics

Faculty of Aerospace Engineering

TU Delft

Delft University of Technology

Numerical Study of Fluid Structure Interaction in Nuclear Reactor Applications

Master of Science Thesis

For obtaining the degree of Master of Science in Aerospace Engineering
at Delft University of Technology

Eline ter Hofstede

August 20, 2015

Faculty of Aerospace Engineering · Delft University of Technology

Delft University of Technology

DELFT UNIVERSITY OF TECHNOLOGY
DEPARTMENT OF AERODYNAMICS

The undersigned hereby certify that they have read and recommend to the Faculty of Aerospace Engineering for acceptance the thesis entitled **"Numerical Study of Fluid Structure Interaction in Nuclear Reactor Applications"** by **Eline ter Hofstede** in fulfillment of the requirements for the degree of **Master of Science**.

Dated: August 20, 2015

Supervisors:

Afaque Shams

Alexander van Zuijlen

David Blom

Roeland de Breuker

Stefan Hickel

Preface

This document is the final report of the Master of Science thesis, and documents the results of the Master Thesis Project. The master thesis project was carried out at the Nuclear Research Group in Petten. The application is therefore nuclear reactors, the used numerical methods can however also be used for other strongly coupled applications.

A project of such duration and scope always has many contributors. Special attention has to be given to the continuous guidance by Sander van Zuijlen and Afaque Shams. Their supervision during the project was greatly appreciated. I would like to thank Vattenfall Research and Development in Sweden for supplying us with their experimental data and Eric Lillberg, Vasilis Papadimitriou and Kajsa Bengtsson for discussing the experiments with me. I also would like to thank David Blom from Delft University of Technology for supplying me with his numerical implementation of the FSI method in OpenFOAM (the FSI-FOAM solver), and being always available for answering my questions about OpenFOAM. Also I would like to thank NRG for allowing me to use their facilities and the support of all the great colleagues. Last but not least I would like to thank my friends and family for supporting me during this project.

Abstract

Flow-induced vibration (FIV) plays an important role in the nuclear industry. In nuclear power plants (NPP), the FIV may cause fatigue problems, stress corrosion cracking, possible failure modes and fretting wear. This in return can lead to nuclear safety issues and substantial stand-still costs due to unplanned outage. The demand for an increase in power density of nuclear reactors often results in the increase of coolant flow velocities or a change of cooling liquid. These changes may alter the flow behaviour, which can lead to fluid-elastic instability. It is therefore important to asses this phenomena early in the design process.

Modelling the onset of FIV involves the simulation of fluid dynamics (CFD) and solid mechanics (CSM) and their interaction. Most of the experimental studies that have been performed previously to predict the onset of FIV are oversimplified or only cover a single operation condition. On the other hand, using a combination of CFD and CSM can play an important role for the complex industrial applications. To gain the confidence of the available numerical methods, their validation is an important step that needs to be performed.

In the present work a validation study is performed on the computational methods used in Fluid-Structure Interaction (FSI) for nuclear plant applications. The numerical simulations are performed using the open source code OpenFOAM Extend, in which both the fluid and structural dynamics are computed using the Finite Volume (FV) method. Moreover, a partitioned approach is used, in which the exchanges between the fluid and structure solver takes place through the use of the Interface Quasi Newton with Inverse Jacobian from a Least-Squares (IQN-ILS) coupling scheme.

The validation consists of several steps:

First the numerical methods were used to simulate a well known benchmark case (Turek, 2006). In this case, the deformation of an elastic flap, attached to a solid cylinder is studied. This case is well suited to validate the used coupling methods for applications with large structural deformations.

After this, the same numerical methods are used to simulate the free vibration of a beam fluid (flow). To validate the use of the numerical methods, the results are then compared to the experimental values.

After this, the validated methods are applied on an industrial application case, where the vibrations of the solid, a scaled version of a neutron flux measurement guide tube, is induced by the turbulent flow.

From this study it is found that the IQN-ILS coupling method can be used for strongly coupled problems. It is also found that the mesh and timestep are important parameters for a correct estimation of the frequency and the damping of the oscillation.

Table of Contents

List of Figures

List of Tables

Chapter 1

Introduction

In the framework of this Master Thesis, a numerical study of the Fluid Structure Interaction (FSI) in nuclear reactor applications is performed. An important part of FSI in nuclear reactor applications are the Flow-Induced Vibrations. In nuclear power plants, FIV may cause fatigue problems, stress corrosion cracking, possible failure modes and fretting wear (Luk, 1993). This in return can lead to nuclear safety issues and substantial stand-still costs due to unplanned outage. Reports of flow-excited failures of heat exchanger tubes began appearing in the 1950s (Weaver, 2000).

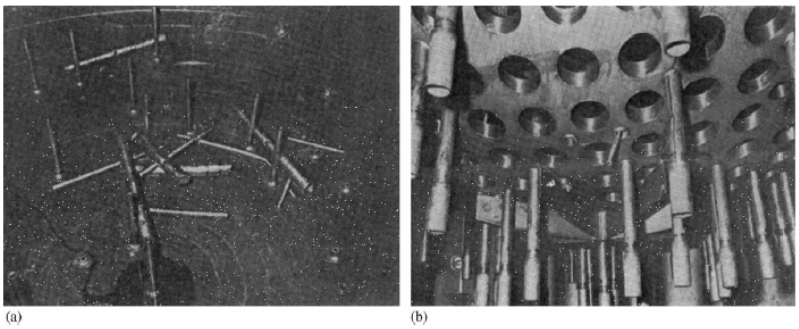

Figure 1.1: Photographs of (a) the bottom of the reactor core showing missing(broken) ICI guide tubes; (b) the bottom of the pressure vessel showing broken ICI nozzles and debris. (Paidoussis, 2006)

An example of the destructive effect of flow induced vibrations is shown in Figure 1.1. In this case flow induced vibration caused a failure of the so-called in-core instrument nozzles and guiding tubes. After a strange noise came from the heat exchanger it was found that 21 out of 42 ICI nozzles had broken off, as well as four In Core Instrumentation (ICI) guide tubes. Some of the parts where carried by the flow towards the heat exchanger, and generated a noise.

Safety always plays an important role in nuclear power plants. But also, the replacement of

components can lead to a long downtime or even shut-down of the concerned units. As was the case for the San Onofre Nuclear Generation Station. FIV led to premature wear in over 3.000 tubes, which caused a leak of radioactive coolant in recently renewed steam generators in Units 2 and 3. Therefore Southern California Edison has decided to permanently close these units. Also many other cases exist where FIV is the major cause of fatigue problems.

The current demand for an increase in power density of nuclear plants often results in the increase of coolant flow, a change of cooling liquid or a change of component material or dimensions. These changes may alter the flow and structural behaviour, and cause flow-induced vibration problems to become more prominent (Weaver, 2000). It is therefore important to assess this phenomenon early in the design process. Because of the need of accurate prediction, FIV is an important area of research.

FIV is an overall term used to describe all the phenomena that are associated with the response of structures immersed in a flow. In nuclear power plants, four dominant vibration-excitation mechanisms can be found, namely: (1) fluid-elastic instability; (2) periodic wake shedding; (3) turbulence-induced excitation; and (4) acoustic resonance (Pettigrew, 1998). When considering the response of a structure to these phenomena, it can be concluded that fluid-elastic instability has the greatest destructive potential (Paidoussis, 2006). However since these phenomena are often related the others should not be overlooked. Since a lot of these phenomena are non-linear it is complex and it is therefore a challenge to model these correctly.

The knowledge and understanding of FIV is critical to estimate the lifetime of the reactor components with regard to fatigue, stress corrosion cracking, possible failure modes and mechanical wear. Or when already installed, the FIV problems can be resolved by eliminating

excitatiut3(.ic415(It)-344Th(ase)-m)-3h.

big while computational time should be minimized. What is the bottle neck of the simulation?

1.2 Approach

Often analytical models are used to predict FIV. Many analytical models for slender bodies in axial flow do not use the full Navier-Stokes equations but split the fluid forces into an inviscid and viscous part. The contributions of the inviscid forces were first derived by Lighthill in 1960 (Lighthill, 1960), while the viscous forces were based on empirical relations, obtained from experiments on specific cases. The downside of doing this is the lack in accuracy when applied to other or less simplified cases. Because of the increase of computational power it becomes more attractive to calculate the flow induced vibration by using a numerical simulation.

The mutual interaction between the fluid flow and the solid is often referred to as Fluid-Structure Interaction (FSI). Solving an FSI problem numerically can be done in multiple ways. One can use a monolithic approach, this means that the equations of the fluid and the solid are written as one set of equations and solved all together. In this way their mutual influence can be taken into account during the solution progress. Using a monolithic approach therefore requires the implementation of a completely new code.

Another way to solve the FSI problem is the partitioned approach. In a partitioned FSI simulation the flow equations and the structural equations are solved with different numerical methods. This gives more freedom in selecting suitable methods for fluid and structural solvers than the monolithic approaches. The partitioned approach requires a coupling algorithm to model the interaction between the fluid and solid at the interface. The partitioned approach can be further divided according to the coupling method used, which makes a difference between loose-coupling and strong-coupling algorithms. If the interaction between the fluid and the structure is weak, a loosely coupled method, i.e. one coupling iteration per time step, can be used. When the interaction is strongly coupled, the solvers are called multiple times during a time step until both the kinematic and the dynamic equilibrium conditions are satisfied.

Using FSI to predict the occurrence of FIV for the development of 4th generation reactors is challenging. Some of these reactors are using a cooling medium with a high density, like lead-bismuth eutectic. In this case the mass ratio of the solid (for example the fuel bundles) and the fluid is low ($\rho_s/\rho_f << 1$) and the added mass, i.e. the mass of fluid which is accelerated by the structure, is large. It is shown that in this case loosely coupled solvers suffer from poor convergence or even instability, therefore a strongly coupled method is necessary (Banksa et al., 2014) (Causin, 2005) (Yang, 2008).

This thesis report validates the use of a strongly coupled partitioned FSI method on a system with a low mass ratio and a large added mass. Two different reference databases are used for the validation procedure. The first is a numerical benchmark case of Turek. In this reference case, the deformation of an elastic flap, attached to a solid cylinder is studied.

This is a strongly coupled case with low mass ratios, and is therefore well suited to validate the used coupling methods for strongly coupled applications. The second reference case is an experiment, performed by Vattenfall, where the damping of the flow along an excited (vibrating) slender tube is studied. Here different fluids (air and water) are used and it therefore enables to validate the used method for different added mass. After this the validated methods are applied on an industrial application.

A short introduction to the flow conditions found in the industrial application, in this case nuclear reactors, is given in Chapter 2. Chapter 3 gives an overview on the used numerical methods. In Chapter 5.4, the validation study is performed, where in section 4.1 it is shown that the IQN-ILS method is able to be used in a simulation of a strongly coupled method. Section 4.2 shows the sensitivity of the solid solver for the mesh size and boundary conditions. Also it is shown that the prediction of the change in frequency caused by the added mass can be correctly obtained. In Chapter 5 an industrial application is shown where the vibration is induced by the turbulent flow. Here the lessons learned with the Validation cases can be applied.

Chapter 2

Nuclear Reactors

This chapter is written to give the reader some background information about nuclear reactors. The numerical methods used in this report are validated, such that they can be applied on nuclear reactor applications. It is therefore useful to know a bit more about the flow conditions and the occurrence of Flow Induced Vibrations in nuclear reactor applications.

2.1 Reactor types

To be able to discuss the typical flows in a reactor a distinction between different kind of reactors has to be made.

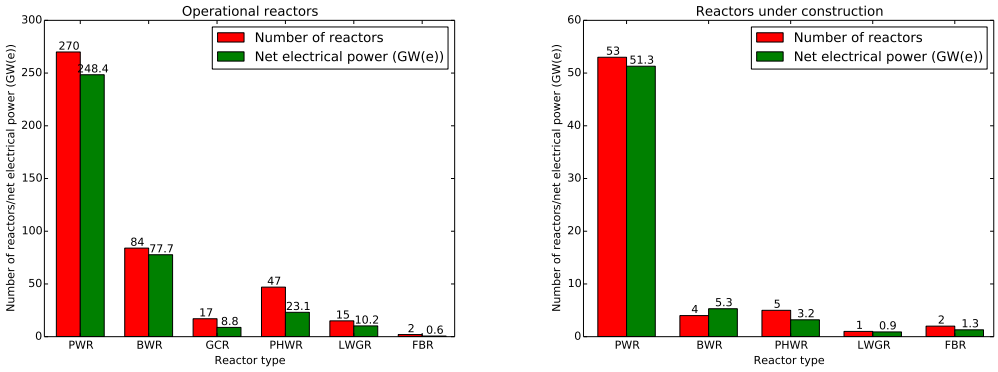

(a) Number of operational reactors

(b) Reactors under construction

Figure 2.1: Types of reactors used and constructed by type and net electrical power (as of 31 Dec. 2011). Amended from(IAEA, 2012)

Figure 2.1 gives an overview of the different type of nuclear reactors that are being used

and constructed nowadays. The most common reactor is the Pressurized Water Reactor (PWR). The other types given in Figure 2.1 are: the Boiling Water Reactor (BWR), the Gas Cooled Reactor (GCR), the Pressurized Heavy Water Reactor (PHWR), Light Water Graphite Reactor (LWGR) and the Fast Breader Reactor (FBR). Compared to the PWR, the pressure in the core of an BWR is lower, and therefore the water in the core reaches its boiling point. A GCR uses a gas instead of water, and the PHWR and LWGR use heavy and light water as a cooling fluid. Since the PWR is the most used nowadays this type is used as an example to describe the basic processes and flows in a reactor. Other types of reactors could still be considered later in the project when for example the effect of a change in cooling fluid, cooling fluid velocities etc. will be assessed.

2.2 Reactor components

Figure 2.2 shows a schematic drawing of a PWR and its typical flow systems.

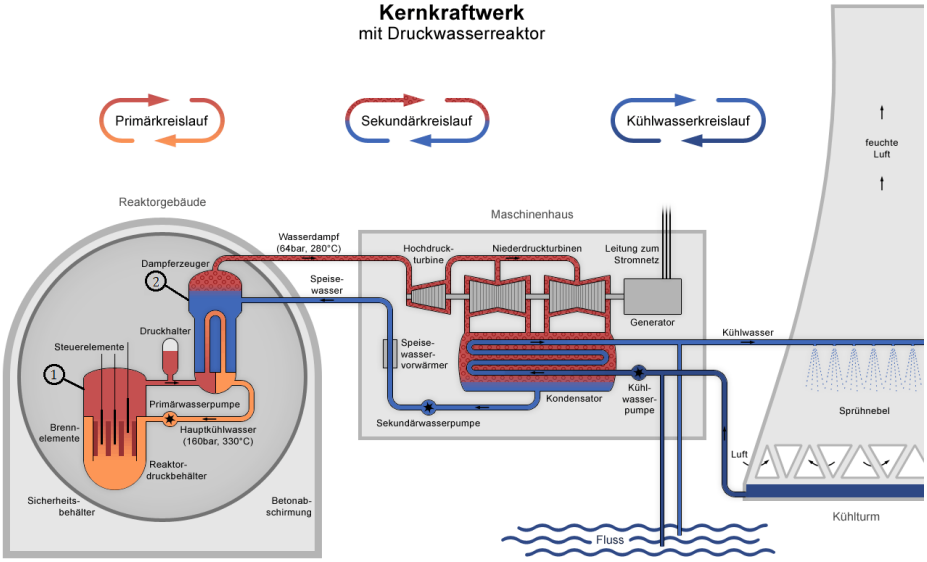

Figure 2.2: PWR diagram (Wikimedia, 2014)

In this study the focus is on regions *one* and *two* , see numbers in Figure 2.2. The assessment of the occurrence of FIV in these regions is essential since a failure can cause the non-radioactive part of the reactor to be contaminated with radio active coolant or cause other high risk situations. Region *one* of Figure 2.2 is called the reactor vessel. The vessel, shown in a bit more detail in Figure 2.3 (a), consists of elements that are commonly found in other types of reactors.

The reactor vessel contains the reactor core and primary coolant. Figure 2.3 (a) also shows the path of the coolant flow. It can be seen that the coolant enters the reactor vessel at the inlet nozzles, called cold legs, and flows downward in the space between the reactor vessel

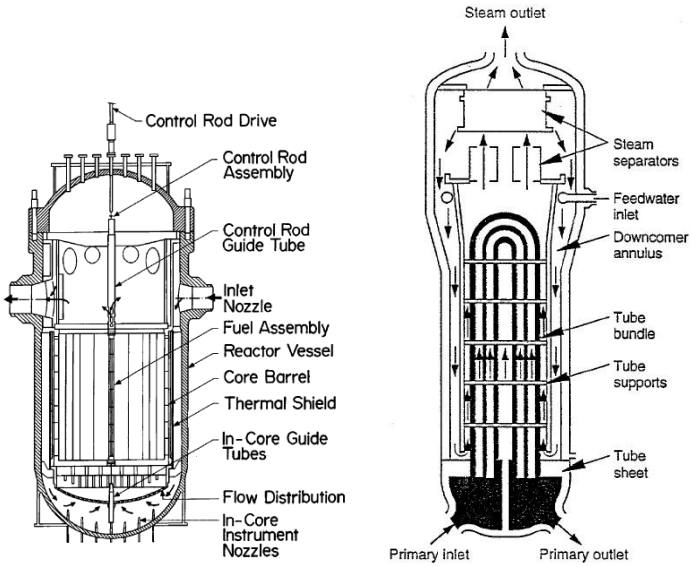

(a) PWR pressure vessel internals

(b) Recirculating steam generator internals

Figure 2.3: Reactor component internals

wall and the core barrel. From the bottom of the reactor vessel, the lower plenum, the flow is turned upward to pass through the fuel assemblies where it flows around and through the fuel assemblies. After this the coolant enters the upper plenum where it is routed out through the outlet nozzles, called hot legs and flows towards the steam generator.

In a PWR the nominal system pressure of the primary cooling system is about 160 bar, therefore the water in the core can reach a temperature of 330° C without starting to boil. The core of the reactor consists of multiple fuel assemblies which contain fuel rods and control rods. The control rods can be used to absorb neutrons to slow down the fuel fission. The fuel rod mainly consists of uranium fuel pellets surrounded by a zirconium cladding. See Figure 2.4 for a detailed representation of the fuel assembly and fuel rod.

A Pressurized Water Reactor (PWR) uses water as a coolant and moderator. The heat produced by the nuclear fission is transported by the coolant from the fuel rods to the steam generators, this cycle is defined as the primary cooling system. The coolant also acts as a neutron moderator, a moderator slows down fast neutrons such that they are more easily absorbed. This will result in an increase of fission which results in an increase of coolant temperature which increases the power of the reactor. The high pressure high temperature water from the primary cooling system goes through a secondary system where steam is generated using heat exchangers (indicated by a *two* in Figure 2.2). After this the steam goes through a turbine to generate electricity. A more detailed picture of (the flow through) the steam generator can be found in Figure 2.3 (b). As can be seen here, the primary flow enters the steam generator at the bottom and travels through the steam generator tubes. Water from the steam separator and the flow from the secondary system (coming from the condenser, trough the feed water inlet) are combined. This flows to the bottom of the steam

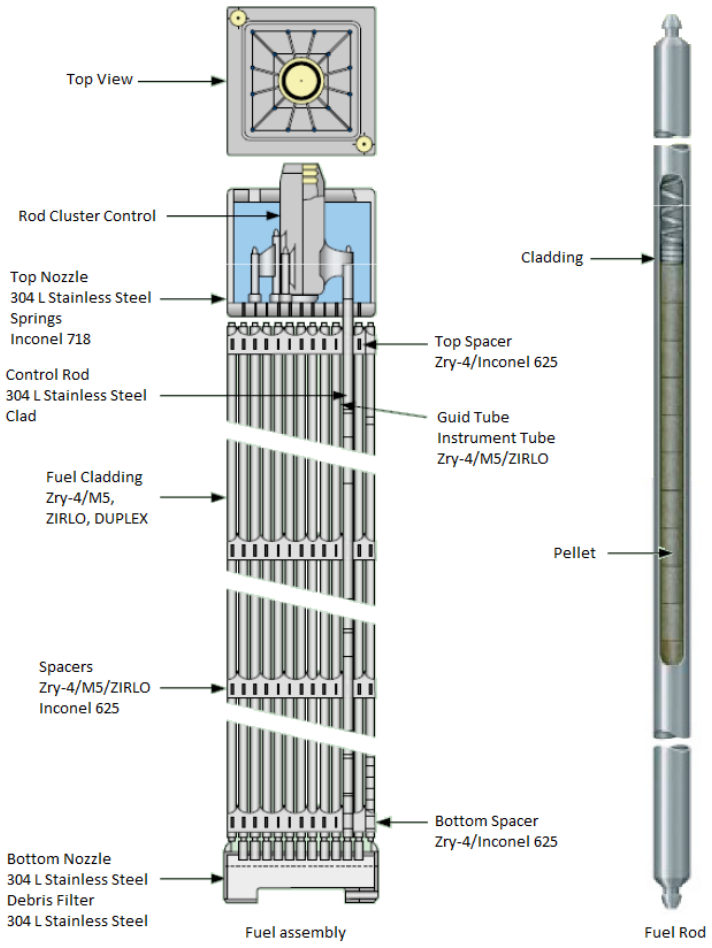

Figure 2.4: PWR fuel assembly

generator and exchanges heat with the steam generator tubes while travelling up. Because of the heat exchanged and the lower pressure (64 bar) in the steam generator (compared to 160 bar in the primary system) the water in the secondary system starts to boil. The steam goes through a steam separator and a steam dryer, which are located in the top part of the steam generator. Now the dried steam travels through the turbines to generate electricity. After this the steam goes through a heat exchanger where it condenses.

2.3 Coolant

As can be seen from Figure 2.1, 62% of all currently operating plants are light water reactors (BWR and PWR), and therefore use ordinary water as a coolant. The heavy water reactors use deuterium oxide, D2O is a weaker moderator than light water but is used because it

absorbs less neutrons, thus offering a better neutron economy. The gas cooled reactors (GCR) use a gas, such as helium or carbon dioxide. Reactors with a high energy density (FBR) are cooled with liquid metals, like molten sodium, lead, or lead bismuth eutectic(LBE), because they operate a fast neutron spectrum.

Table 2.1: Density ratios fluid and solid

Reactor	$\rho_f[kg/m^3]$	$\rho_{zirconium}(6520)/\rho_f$	$\rho_{steel}(8000)/\rho_f$
BWR and PWR			
Light water (H2O)	970 (300 C 160 bar)	6.7216	8.2474
PHWR			
Heavy water (D2O)	1105.6	5.9005	7.2398
GCR			
Carbon dioxide (CO2)	10.87 (400C, 150 atm)	652	800
Helium (He)	119.52 (400 C, 150 atm)	66.93	54.55
FBR			
Sodium	750 (at 1100 K)	8.69	10.67
lead	10100 (at 1100 K)	0.646	0.792
LBE	9700 (at 1100 K)	0.672	0.825

The density ratio, the ratio of the density of the solid over the density of coolant (ρ_s/ρ_f) for most plants is low (< 10). Table 2.1 gives an overview of the different plants with their density ratio. Two different solids are taken, zirconium and steel. Zirconium is often used as the fuel cladding where steel is often used as core structural material (IAEA) and for example for the housing of measurement instruments inside the core. In FBR reactors using lead or LBE as a moderator, the density ratio smaller than one, this means that the density of the fluid is larger than the density of the solid.

2.4 Flow excitation mechanisms

The term Flow Induced Vibration (FIV) is used to describe all the phenomena that are associated with the response of structures immersed in a flow. To be able to study FIV, first the most common flow conditions in the nuclear components should be identified.

As can be seen in Figure 2.3, axial flow generally prevails along the fuel elements whereas in the steam generator both axial and cross flow play a role. The type of flow along the fuel elements (gas, liquid, or multiphase) depends on the type of reactor. In a PWR the flow through the fuel assembly is liquid. For the recirculating type steam generator (as in Figure 2.3 (b)) the flow at the shell side is liquid at the bottom and becomes two-phase as boiling takes place.

Four different vibration excitation mechanisms can be found in nuclear components namely: (1) fluidelastic instability; (2) periodic wake shedding; (3) turbulence-induced excitation; and (4) acoustic resonance (Pettigrew, 1998). Figure 2.5 relates the vibration excitation mechanisms to different flow situations in the reactor and their relative importance. When

Flow situation	Fluidelastic instability	Periodic shedding	Turbulence excitation	Acoustic resonance
Axial flow				
Internal				
Liquid	*	—	**	***
Gas	*	—	*	***
Two-phase	*	—	**	*
External				
Liquid	**	—	**	***
Gas	*	—	*	***
Two-phase	*	—	**	*
Cross flow				
Single cylinders				
Liquid	—	***	**	*
Gas	—	**	*	*
Two-Phase	—	*	**	—
Tube Bundle				
Liquid	***	**	**	*
Gas	***	*	*	***
Two-phase	***	*	**	—

***Most important.
**Should be considered.
*Less likely.
—, Does not apply.

Steam generator
Fuel rods
Steam generator and fuel rods

Figure 2.5: Vibration excitation mechanisms (amended from (Pettigrew, 1998))

only considering the flow situation in the steam generator and the fuel rods (region *one* and *two* of Figure 2.2) some specific areas in the table can be highlighted. In the steam generator and the fuel rods the dominant excitation mechanisms are considered to be acoustic resonance and fluidelastic instability. A short explanation of the different vibration excitation mechanisms is given here.

1. Fluidelastic instability depends on the coupling between the fluid dynamic forces and the elastic structural displacements. When the energy from the fluid dynamic forces is higher than the energy dissipated by damping, instability occurs.

2. Periodic wake shedding often occurs immediately downstream of structures subjected to cross flow. When periodic wake shedding occurs periodic fluid forces are generated. Resonance may occur if the periodicity of the fluid forces coincides with the natural frequency of the structure.

3. Turbulent excitation can come from far field turbulence. This means that the structure (for example the tube bundles) will absorb energy from the turbulence induced by other structures in front of the tube bundles. Therefore the tubes will experience the turbulence as a forced oscillation.

4. Acoustic resonance occurs when the periodic wake shedding frequency coincides with the natural frequency of the acoustic cavity formed by the structures surrounding the tube bundle.

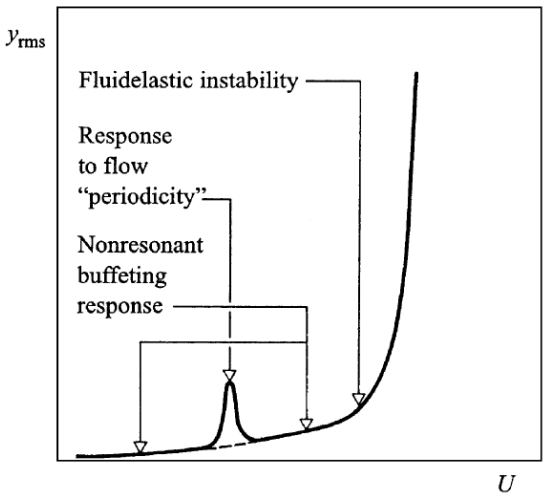

Figure 2.6: Generic idealized response with increasing flow velocity of a structure in either axial or cross-flow (Paidoussis, 2006)

Figure 2.6 shows a generic idealized response of a structure in either axial or cross flow. From this it can be seen that different excitation mechanisms all have a different response. From this it can be concluded that fluid elastic instability has the greatest destructive potential. The other excitation mechanisms can however contribute to the onset of fluid-elastic instability, the different excitation mechanism can be therefore not totally be seen separately.

Chapter 3

Numerical Methods

For the calculation of fluid structure interaction, several numerical methods have to be used to solve for the fluid equations and the structure equations. When using a partitioned approach, the fluid and solid equations are solved with different numerical methods. In this case the fluid domain is solved using a computational fluid dynamic (CFD) method and the solid using a Computational Solid Mechanics (CSM) method. To be able to model the interaction of these two models, the two methods are coupled at the fluid-solid interface. A stable and efficient numerical technique is essential for the study of fluid-structure interaction (FSI). When the interaction is strongly coupled, the solvers are called multiple times during a time step until both the kinematic and the dynamic equilibrium conditions are satisfied.

3.1 Governing Fluid Equations

The governing equations for a flow, i.e. the Navier-Stokes equations, are the conservation of mass and momentum. For an incompressible fluid these relations are given by:

$$\nabla \cdot \boldsymbol{v} = 0, \tag{3.1}$$

$$\rho \left(\frac{\partial \boldsymbol{v}}{\partial t} + \nabla \cdot (\boldsymbol{v}\boldsymbol{v}) \right) = \nabla \cdot \boldsymbol{\sigma} + \boldsymbol{f}, \tag{3.2}$$

with $\boldsymbol{v}$ being the fluid velocity, the fluid density, t the time, $\boldsymbol{\sigma}$ the fluid stress tensor, and $\boldsymbol{f}$ are the body forces, e.g. due to gravity. In this study the body forces are taken to be zero.

For Newtonian fluids, the stress tensor can be written as:

$$\boldsymbol{\sigma} = -p\boldsymbol{I} + \mu\left[\nabla\boldsymbol{v} + (\nabla\boldsymbol{v})^T\right], \tag{3.3}$$

with p the pressure and μ the fluid dynamic viscosity. To solve the equations at the boundaries, velocity boundary condition is used at the inlet, and a pressure is specified at the outlet. At the walls a no slip boundary condition is used, so fixed value zero for velocity and zero gradient for the pressure.

3.2 Governing Solid Equations

The deformation of an elastic incompressible structure is governed by the conservation of momentum:

$$\rho\frac{\partial^2\boldsymbol{d}}{\partial t^2} = \nabla\cdot\boldsymbol{\sigma} + \boldsymbol{f}, \tag{3.4}$$

with $\boldsymbol{d}$ being the structural displacement, ρ the solid density, $\boldsymbol{\sigma}$ the solid stress tensor and $\boldsymbol{f}$ the body forces. In this study the body forces are taken to be zero. When a fixed boundary condition is set the displacement $\boldsymbol{d} = 0$, while if a normal displacement is fixed $\boldsymbol{d}\cdot\boldsymbol{n} = 0$.

3.3 Coupling of the Fluid and Solid Equations

At the interface between the solid and the fluid, the kinematic condition requires the velocity of the fluid to be equal to the time derivative of the displacement of the solid interface:

$$\frac{\partial\boldsymbol{d}_s}{\partial t} = \boldsymbol{v}_f. \tag{3.5}$$

The dynamic condition requires the stress on the interface due to the fluid and solid surface normal to be equal, also called as equality of traction:

$$\boldsymbol{\sigma}_s\cdot\boldsymbol{n}_s = -\boldsymbol{\sigma}_f\cdot\boldsymbol{n}_f. \tag{3.6}$$

The code that solves the structure equations is called the structural solver S and the code that solves the fluid equations is called the flow solver F. When using a Dirichlet-Neumann decomposition, the flow equations can be solved for a given velocity (or displacement) of the fluid-structure interface (Dirichlet boundary condition), and the solid equations are solved for a given traction distribution on the interface (Neumann boundary condition). Taking $\boldsymbol{x} = \boldsymbol{d}_s$ and $\boldsymbol{y} = \boldsymbol{\sigma}_f \cdot \boldsymbol{n}_f$, the response of the structure solver can be therefore written as:

$$\boldsymbol{x} = S(\boldsymbol{y}). \tag{3.7}$$

The response of the fluid solver can now be written as:

$$\boldsymbol{x} = S \circ F(\boldsymbol{x}), \tag{3.8}$$

where $S \circ F$ is the result of function F is given as argument to the function S. Since the flow equations and the structural equations are solved separately, a residual at the interface can be found:

$$\boldsymbol{r}(\boldsymbol{x}) = S \circ F(\boldsymbol{x}) - \boldsymbol{x}, \tag{3.9}$$

To reach convergence, this residual should be minimized, which can be done using an optimization algorithm. Well known approaches in FSI are the Gauss-Seidel method (Simth et al., 1996), fixed under-relaxation, Aitken under-relaxation (Kuttler and W., 2008), and the IQN-ILS method (Degroote et al., 2010).

3.3.1 IQN-ILS

The Interface Quasi-Newton with Inverse Jacobian from a Least Squares (IQN-ILS) is an efficient algorithm for strongly coupled problems (De Ridder and Degroote, 2013) (Degroote, 2013). The IQN-ILS method is an Interface Quasi-Newton with an approximation of the Inverse of the Jacobian for a Least Squares approximation. The IQN-ILS is a coupling technique that can also be used when both the flow solver and the structural solver are treated as a black box. In the current study the IQN-ILS method (Degroote et al., 2010) (Degroote et al., 2009) is applied. This section gives a discription of the IQN-ILS method, taken from (Degroote et al., 2010).

To minimize the residual, equation (3.9) can be written as

$$\boldsymbol{r}(\boldsymbol{x}) = S \circ F(\boldsymbol{x}) - \boldsymbol{x} = 0, \tag{3.10}$$

this non-linear equation in $\boldsymbol{x}$ can be solved using quasi-Newton iterations, where the dependence of $\boldsymbol{r}$ on $\boldsymbol{x}$ is further omitted for clarity,

$$\widehat{\frac{d\boldsymbol{r}}{d\boldsymbol{x}}|_{\boldsymbol{x}^k}} \Delta \boldsymbol{x}^k = -\boldsymbol{r}^k, \tag{3.11}$$

$$\boldsymbol{x}^{k+1} = \boldsymbol{x} + \Delta \boldsymbol{x}^k, \tag{3.12}$$

where the hat is used to indicate the approximation of the Jacobian. This approximation is necessary because the exact Jacobian of $\boldsymbol{r}(\boldsymbol{x})$ is unknown as F and S are taken as black-box functions, and are therefore unavailable. In each quasi-Newton iteration,the residual vector is calculated as the output of the structural solver ($\boldsymbol{x}_s^{k+1}$) minus the input of the flow solver ($\boldsymbol{x}_f^k$)

$$\boldsymbol{r}^k = \boldsymbol{R}(\boldsymbol{x}^k) = S \circ F(\boldsymbol{x}^k) - \boldsymbol{x}^k = \boldsymbol{x}_s^{k+1} - \boldsymbol{x}_f^k. \tag{3.13}$$

The linear system of equation (3.11), has the same dimension as the number of degrees-of-freedom as the interface's displacement, and has to be solver in each quasi-Newton iteration. Although the number of degrees-of-freedom in the interface's displacement is generally smaller than the number of degrees-of-freedom of the entire fluid and structure domain, the Jacobian matrix $d\boldsymbol{r}/d\boldsymbol{x}$ is usually dense. As a result, the solution of the linear system corresponds to a significant computational cost in large simulations. It is therefore more advantageous to approximate the inverse of the Jacobian by applying the least-squares technique on a particular set of vectors.

By approximating the inverse of the Jacobian the quasi-Newton iterations (equations (3.11) and (3.12)) can be written as

$$\boldsymbol{x}^{k+1} = \boldsymbol{x}^k + \left(\widehat{\frac{d\boldsymbol{r}}{d\boldsymbol{x}}|_{\boldsymbol{x}^k}} \Delta \boldsymbol{x}^k \right)^{-1} \left(-\boldsymbol{r}^k \right). \tag{3.14}$$

The approximation for the inverse of the Jacobian does not have to be created explicitly; a procedure to calculate the product of this matrix with the vector $-\boldsymbol{r}^k$ is sufficient. The vector $-\boldsymbol{r}^k$ is the difference between the desired residual, i.e. $\mathbf{0}$, and the current residual $\boldsymbol{r}^k$ and it is further denoted as $\Delta\boldsymbol{r} = \mathbf{0} - \boldsymbol{r}^k$. The correction of the displacement in equation (3.14) is rewritten as

$$\Delta\boldsymbol{x}^k = \left(\widehat{\frac{d\boldsymbol{r}}{d\boldsymbol{x}}|_{\boldsymbol{x}^k}\Delta\boldsymbol{x}^k}\right)^{-1}\left(-\boldsymbol{r}^k\right) \approx \widehat{\frac{d\boldsymbol{x}}{d\boldsymbol{r}}}\left(-\boldsymbol{r}^k\right), \tag{3.15}$$

with a slight abuse of notation. After substitution of the definition of the residual $\boldsymbol{r} = \boldsymbol{x}_s - \boldsymbol{x}_f$, this becomes

$$\Delta\boldsymbol{x}^k \approx \widehat{\frac{d\boldsymbol{x}}{d\boldsymbol{r}}}\left(-\boldsymbol{r}^k\right) = \left(\widehat{\frac{d\boldsymbol{x}_s}{d\boldsymbol{r}}} - \boldsymbol{I}\right)\left(-\boldsymbol{r}^k\right) = \widehat{\frac{d\boldsymbol{x}_s}{d\boldsymbol{r}}}\left(-\boldsymbol{r}^k\right) + \boldsymbol{r}^k. \tag{3.16}$$

This indicates that the change $\Delta\boldsymbol{x}_s$ of the structural solver's output due to a given change of the residual $\Delta\boldsymbol{r} = -\boldsymbol{r}^k$

$$\Delta\boldsymbol{x}_s = \widehat{\frac{d\boldsymbol{x}_s}{d\boldsymbol{r}}}\left(-\boldsymbol{r}^k\right) \tag{3.17}$$

has to be approximated. This is done with date obtained during the previous quasi-Newton iterations; equation (3.13) shows that the flow equations and the structural equations are solved in quasi-Newton iteration k, resulting in $\boldsymbol{x}_s^{k+1} = S \circ F(\boldsymbol{x}^k)$ and the corresponding residual $\boldsymbol{r}^k$. To predict how $\boldsymbol{x}_s$ changes when $\boldsymbol{r}$ changes, these vectors are converted into difference with respect to the first quasi-Newton iteration.

$$\Delta\boldsymbol{r}^k = \boldsymbol{r}^k - \boldsymbol{r}^0 \tag{3.18}$$

$$\Delta\boldsymbol{x}_s^{k+1} = \boldsymbol{x}_s^{k+1} - x_s^1. \tag{3.19}$$

Each quasi-Newton iteration generates an additional vector $\Delta\boldsymbol{r}$ and the corresponding vector $\Delta\boldsymbol{x}_s$. These vectors are stored as the columns of the matrices

$$\boldsymbol{V}^k = \begin{bmatrix}\Delta\boldsymbol{r}^{k-1} & \Delta\boldsymbol{r}^{k-2} & \cdots & \Delta\boldsymbol{r}^1 & \Delta\boldsymbol{r}^0\end{bmatrix} \tag{3.20}$$

and

$$\boldsymbol{W}^k = \begin{bmatrix} \boldsymbol{x}_s^k & \boldsymbol{x}_s^{k-1} & \cdots & \boldsymbol{x}_s^2 & \boldsymbol{x}_s^1 \end{bmatrix} \tag{3.21}$$

The number of columns in $\boldsymbol{V}^k$ and $\boldsymbol{W}^k$ is indicated as v, and is generally much smaller than the number of rows u. The desired change of the residual $\Delta\boldsymbol{x} = \boldsymbol{0} - \boldsymbol{r}^k$ is approximated as

$$\Delta\boldsymbol{r} \approx \boldsymbol{V}^k \boldsymbol{c}^k \tag{3.22}$$

with $\boldsymbol{c}^k \in \mathbb{R}^{\tilde{\approx}}$ the coefficients of the decomposition. Because $v \leq u$, equation (3.22) is an overdetermined set of equations for the elements of $\boldsymbol{c}^k$ and hence the least-squares solution to this linear system is calculated. Therefore, the so-called economy size QR-decomposition of $\boldsymbol{V}^k$ is calculated using Householder transformations

$$\boldsymbol{V}^k = \boldsymbol{Q}^k \boldsymbol{R}^k, \tag{3.23}$$

where the coefficient $\boldsymbol{c}^k$ can than be determined by solving

$$\boldsymbol{R}^k \boldsymbol{c}^k = \boldsymbol{Q}^{kT} \Delta\boldsymbol{r}, \tag{3.24}$$

using back substitution. The $\Delta\boldsymbol{x}_s$ that corresponds to $\Delta\boldsymbol{r} \approx \boldsymbol{V}^k\boldsymbol{c}^k$ can be approximated using the same decomposition coefficients $\boldsymbol{c}^k$ but with respect to W^k because there is a one-to-one relation between the columns of $\boldsymbol{V}^k$ and $\boldsymbol{W}^k$, so

$$\Delta\boldsymbol{x}_s = \boldsymbol{W}^k \boldsymbol{c}^k. \tag{3.25}$$

When substituting this in equation (3.16) gives

$$\Delta\boldsymbol{x} = \boldsymbol{W}^k \boldsymbol{c}^k + \boldsymbol{r}^k. \tag{3.26}$$

Since $\boldsymbol{V}^k$ and $\boldsymbol{W}^k$ have to have to contain atleast one column, a relaxation with factor ω is performed in the second coupling iteration of each time step. Because of similarity between consecutive time steps, information from former time steps can be reused.

The algorithm can be summarized with the pseudo code as:

$k = 0$
$x_s^1 = S \circ F(\boldsymbol{x}^0)$
$\boldsymbol{r}^0 = \boldsymbol{x}_s^1 = \boldsymbol{x}^0$
while $||\boldsymbol{r}^k||_2 > \epsilon_0$ ***do***
  if $k = 0$ ***then***
    $\boldsymbol{x}^{k+1} = \boldsymbol{x}^k + \omega \boldsymbol{r}^k$
  else
    construct $\boldsymbol{V}^k$ *and* $\boldsymbol{W}^k$ *using Equations 3.20 and 3.21*
    calculate $\boldsymbol{V}^k = \boldsymbol{Q}^k \boldsymbol{R}^k$
    solve $\boldsymbol{R}^k \boldsymbol{c}^k = -\boldsymbol{Q}^{kT} \boldsymbol{r}^k$
    $\boldsymbol{x}^{k+1} =^k + \boldsymbol{W}^k \boldsymbol{c}^k + \boldsymbol{r}^k$
  end *if*
  k=k+1
  $x_s^{k+1} = S \circ F(\boldsymbol{x}^k)$
  $\boldsymbol{r}^k = x_s^{k+1} - x^k$
end ***while***

3.3.2 Added Mass

When evaluating a problem where fluid is flowing past a hollow tube (cylinder), the added mass can be seen as fluid sticking to the surface of the cylinder adding mass to the cylinder, hence added mass. The inertia of the fluid will therefore also influence the natural frequency of the structure. The effective tube mass is the sum of structural mass and fluid-added mass (Thulukkanam, 2000):

$$m = m_a + m_f = \chi \frac{\pi D^2 \rho_f}{4} + \frac{\pi (D^2 - D_i) \rho_s}{4} \tag{3.27}$$

where ρ_f is the fluid density, ρ_s is the tube material density and D and D_i the tube diameter and tube inner diameter. So the added mass is defined as the displaced fluid mass times a coefficient χ.

The added mass for a single circular cylinder in an unconfined flow is ρA. If the flow is confined the added mass will increase, and accounted for by the confinement parameter χ. This coefficient depends on for example the tube array geometry, or tube confinement, and is often determined using experiments. The added mass is an important parameter since an increase in the added mass can destabilize the system (Weaver, 2000).

3.4 Mesh movement

FSI computations involve moving boundaries for the flow due to the deformation of the structure. A straight forward method to solve this problem is complete regeneration of the mesh. However when doing this the conservation laws are lost and regenerating the complete mesh can be time consuming. Different (more efficient) mesh deformation methods can be defined (Bijl, 2008): Transfinite interpolation, Master-slave coupling, Spring analogy, Least squares, Solid body elasticity, Laplacian smoothing,Biharmonic operator and the Radial Basis Function (RBF).

The radial basis function is a method that can give accurate results with moderate calculation times, and is therefore often used. The RBF interpolation method is based on spline functions, in which the argument depends on the Euclidean distance between the center $\boldsymbol{x}_c$ and its neighbours $\boldsymbol{x}$: $\|\boldsymbol{x} - \boldsymbol{x}_c\|$. The interpolation can be acquired by use of the following expression:

$$\boldsymbol{w}_i(\boldsymbol{x}) = \sum_{j=1}^{n_A} \gamma_j \phi\left(\left\|\boldsymbol{x} - \boldsymbol{x}_{Aj}\right\|\right) + q(\boldsymbol{x}) \quad i = \{A, B\}, \quad \boldsymbol{w} = \{\boldsymbol{u}, p\boldsymbol{n}\} \tag{3.28}$$

where $\boldsymbol{x}_{Aj}$ are the values of the centres of mesh A, q a polynomial, and ϕ the given RBF. Although several RBFs exist, the thin plate spline is used here

$$\phi(r) = r^2 \ln(r). \tag{3.29}$$

3.5 Software package

This study is performed using the software package OpenFOAM Extended, with the FOAM-FSI libraries. FOAM-FSI is an OpenFOAM implementation of FSI solvers by David Blom et al, from the Delft University of Technology. OpenFOAM Extended is a fork of OpenFOAM and is a free, open source CFD software package with also some capabilities to solve CSM. The advantages of using OpenFOAM instead of a (combination of) commercial tools will be that the number of calculations is not limited to the available licences. Also, since the code is freely accessible it is easier to check or implement methods. However since OpenFOAM is an open-source code not all the implemented models are validated. Also the limited amount of available documentation and the lack of quality control makes for the necessity of validation of this specific tool before it can be implemented for industrial projects.

3.6 Discretization Schemes

Different discretization methods can be used to represent and evaluate the equations in a specific volume. The most common methods are finite difference, finite volume, and finite elements. The finite difference method is a collocation method that uses the Taylors series expansion, the finite volume method uses an integral formulation based on conservation laws and the finite element method is a weighted residual method based on local basis functions.

Most commercial codes used to solve solid mechanics use the Finite Element Method (FEM), while fluid mechanics codes usually use the Finite Volume (FV) method. In OpenFOAM both the fluid and structure equations are discretized using the Finite Volume Method. It is shown that for non-linear Computational Solid Mechanics (CSM) problems FV methods are competitive with FE discretisations in terms of numerical accuracy and speed of solution (Slone et al., 2003). Equation (3.2), has a temporal term, a convection term and a diffusion term. The schemes used to solve for this terms are described in the following subsections.

3.6.1 Spatial discretization

When using the finite volume method the computational domain is divided in smaller control volumes on which the conservation laws are imposed. These smaller volumes are commonly referred to as the cells or the grid of the computational domain. The spatial derivative terms are integrated over the cell volume after which Gauss theorem is used to convert this into integrals over the cell surfaces bounding the volume.

The grid size can have a big influence on the accuracy of the solution. When the cell size approaches zero the simulation approaches the exact solution of the differential equations. In OpenFOAM the discretization and interpolation schemes are implemented in the fvSchemes dictionary.

3.6.2 Interpolation scheme

OpenFOAM uses a collocated grid. This means that all unknowns are defined at the centre of the cell. The interpolation schemes are used to interpolate values typically from cell centres to face centres.

Linear interpolation

For a linear convection differencing scheme the values ϕ_f are interpolated from the cell centres to the cell faces. For a linear scheme the values at the cell face can be calculated using

(de Oliveira Samel Moraes et al., 2013):

$$\phi_f = f_x \phi_P + (1 - f_x)\phi_N \tag{3.30}$$

where ϕ_N is the value in the neighbouring cell center and ϕ_P the value in the owner cell, and

$$f_x = \frac{\overline{fN}}{\overline{PN}}, \tag{3.31}$$

$\overline{fN}$ is the distance between the face centroid, f, and the centroid of element N and $\overline{PN}$ is the distance between the centroids of the P and N elements. In many cases linear interpolation will be effective.

An error during the interpolation can be introduced due to the skewness of the cells. To calculate the value of the face integrals the variable in the middle of the face is needed, however with skewed cells this midpoint can be determined incorrectly. In this case a skew correction is necessary, in OpenFOAM this is for example the *'skewCorrected linear'* scheme, which is Skewness-corrected interpolation scheme that applies an explicit correction to the linear scheme.

Rhie-Chow interpolation

To overcome the saddle point problem of the discretized block coupled system of equation Rhie-Chow interpolation technique can be used. Rhie-Chow (Rhie and Chow, 1983) interpolation uses a local correction of the pressure gradient to calculate the face flux. Using this technique a staggered-grid discretization is imitated, where the discrete mass conservation equation is expressed in terms of the discrete mass fluxes across the cell faces.

Gradient Schemes

For structured grids the gradient of a scalar at a given control volume centroid can be easily computed using the definition of the derivative. However when solving for unstructured grids, the usual approach is to make use of the Green-Gauss theorem,

$$\int_\Omega \nabla\phi \, d\Omega = \int_S \phi \, \hat{n} \, dS \tag{3.32}$$

The integral over the surface can be approximated as a summation of the average scalar value

in each face time the face surface vector

$$\nabla\phi_P = \frac{1}{\Omega}\sum_{faces}\phi_f\,\boldsymbol{S}_f \tag{3.33}$$

So the Gauss keyword specifies the standard finite volume discretisation of Gaussian integration, however this requires the interpolation of values from cell centres to face centres. Therefore, the Gauss entry must be followed by the choice of interpolation scheme, like for example linear (see section 3.6.2).

Surface normal gradient schemes

A surface normal gradient, is a gradient ∇ evaluated at a cell face calculated normal to the face. When the *corrected* scheme is used, a correction is made for the angle between the face normal vector, $\boldsymbol{s}_f$, and the element center-to-center vector $\overline{PN}$.

Laplacian schemes

A typical Laplacian term found in fluid mechanics is $\nabla\cdot(\nu\nabla\boldsymbol{U})$. In OpenFOAM the Gauss discretization scheme is used to solve the Laplacian (∇^2), and requires a selection of the interpolation scheme for the diffusion coefficient (for example ν) and a surface normal gradient scheme (to solver for example $\nabla\boldsymbol{U}$). See subsection 3.6.2 and subsection 3.6.2 for the description of the interpolation and normal gradient schemes.

3.6.3 Temporal discretization

For transient simulation discretization schemes are necessary for both space and time. Where the space is discretized using a mesh the time is discretized in (time) steps. In a consistent scheme, when the time step is going to zero the exact solution is approached.

An implicit first order backward differencing scheme can be written as:

$$\left(\frac{\partial\phi}{\partial t}\right)^{n+1} = \frac{\phi^{n+1}-\phi^{n}}{\Delta t} + \mathcal{O}(\Delta t) \tag{3.34}$$

And a seconder order implicit scheme:

$$\left(\frac{\partial\phi}{\partial t}\right)^{n+1} = \frac{3\phi^{n+1}-4\phi^{n}+\phi^{n-1}}{2\Delta t} + \mathcal{O}(\Delta t^2) \tag{3.35}$$

A explicit first order forward differencing scheme can be written as:

$$\left(\frac{\partial \phi}{\partial t}\right)^n = \frac{\phi^{n+1} - \phi^n}{\Delta t} + \mathcal{O}(\Delta t) \tag{3.36}$$

To solve the solid equation the difference approximation of higher order derivatives are needed. A forward difference approximation of the second order derivative of ϕ is given by

$$\frac{\partial^2 \phi}{\partial t^2} = \frac{\phi^{n+1} - 2\phi^n + \phi^{n+1}}{\Delta t^2} + \mathcal{O}(\Delta t). \tag{3.37}$$

In this report the first order bounded implicit (Euler) scheme and the second order implicit scheme are used for the solid and a second order backward is used for the fluid.

3.7 Linear solvers

There are multiple methods to obtain the numerical solution of linear systems ($\boldsymbol{Ax} = \boldsymbol{b}$). The solvers available in OpenFOAM are (OpenFOAM, 2013):

- PBiCG - preconditioned bi-conjugate gradient solver for asymmetric matrices
- PCG - preconditioned conjugate gradient solver for symmetric matrices
- GAMG - generalised geometric-algebraic multi-grid solver
- smoothSolver - solver using a smoother for both symmetric and asymmetric matrices
- diagonalSolver - diagonal solver for both symmetric and asymmetric matrices

The preconditioners include the diagonal incomplete-Cholesky (DIC) and diagonal incomplete LU (DILU), and a GAMG preconditioner amongst others. The smoothers include DIC, DILU and Gauss-Seidel; variants of DIC and DILU exist with additional Gauss-Seidel smoothing.

3.8 Elastic Non Linear Total Lagrangian Solid Solver

The solid solver used in this report is the *'elasticNonLinTLSolidFoam'* solver in OpenFOAM. This finite volume structural solver uses a total strain total Lagrangian approach, and is valid for finite strains, finite displacements and finite rotations. In the total Lagrangian approach

the discrete equations are formulated with respect to the reference configuration. Using this solver the stress-strain relation is elastic and non-linear. The total strain is calculated by separately calculating the volumetric strain and shear strain.

3.9 Fluid solver

The finite volume methods can solved using an uncoupled or a coupled solver. With a uncoupled solver, the system of partial differential equations are solved one at a time for all cells. In the case of a coupled solvers all equations are solved and than repeated for all cells. In a block-coupled solver a single matrix is assembled with all fields and equations.

When using a segregated solver, a pressure velocity coupling of the implicitly discretized fluid flow equations on a collocated grid in OpenFOAM is needed. In this project the pressure-implicit split-operator algorithm, or PISO-algorithm (Issa, 1986) is used. In case of an incompressible flow, the PISO-algorithm first performs a predictor step after which two corrector steps are performed.

In the predictor step the pressure field at t^{n+1} is used to solve the momentum equation, resulting in an intermediate velocity field. This velocity field will in general not satisfy the continuity equation. In the first corrector step a pressure equation is solved to obtain an intermediate pressure field. Using this pressure field the momentum equation is solved again, resulting in a new velocity field which satisfies the continuity equation. In the second corrector step the first corrector step is repeated, yielding a final pressure and velocity field. More corrector steps can be performed which will improve the accuracy.

3.10 Turbulence modelling

The application case considered for the present study is the industrial application. The experimental study of this case has shown that the resulting vibration in the structure is induced by the turbulent flow field. Hence, a good prediction of the turbulence is quite important for this very case. Among the available turbulence modelling approaches are (Unsteady) Reynolds Averaged Navier Stokes ((U)RANS), hybrid (RANS with LES), Large Eddy Simulation (LES) and Direct Numerical Simulation (DNS). In (U)RANS the Navier Stokes equations are time averaged and therefore do not seem to be a good approach for modelling the flow induced vibrations. The hybrid approach uses the (U)RANS model in the near wall region and LES for the bulk, which again will not be suitable for modelling FIV here. Therefore a high fidelity method is needed, like LES or DNS. Among them, DNS will be computationally too expensive. As a result LES is taken as turbulence modelling approach.

In LES, the size of the turbulence scales are determined by the grid resolution, so the smallest grid size determines the smallest scale that can be resolved. Where the large scales are the turbulent scales that can be explicitly solved using a given grid size. The smaller scales

are than solved using a sub-grid-scale (SGS) model. LES uses Kolmogorovs theory of self similarity, where the large eddies of the flow are dictated by the geometry and boundary conditions of the flow, while the smaller eddies tend to be more isotropic. The large scales are therefore directly resolved, whereas the smaller eddies are modelled. LES uses filtering of the Navier-Sokes equations to obtain the turbulent stress tensor (τ_{ij}), which represents the sub-grid scale stresses and is defined as:

$$\tau_{ij} - \frac{1}{3}\tau_{kk}\delta_{ij} = -2\mu_t \overline{S}_{ij} \tag{3.38}$$

where μ_t is the SGS turbulent viscosity and $\overline{S}_{ij}$ is the rate of strain tensor. The SGS model used to model the SGS turbulent viscosity μ_t is the Vreman model (Vreman, 2004).

Chapter 4

Validation Study

Two different reference databases are used for the validation procedure. The first is a numerical benchmark case of Turek (Turek, 2006). In this reference case, the deformation of an elastic flap, attached to a solid cylinder is studied. This case is well suited to validate the IQN-ILS method for applications with large structural deformations and low density ratios (ρ_s/ρ_f). The second one is an experiment, performed by Vattenfall (Vu and Truc, 2014), where the oscillation of excited (vibrating) slender tube is studied. With this, the IQN-ILS method can be validated for the use on a more realistic application, which is closer to the conditions of the industrial application. Parts of the work in this chapter is published in the accepted conference paper (Hofstede and Shams, 2015).

4.1 Turek strongly coupled benchmark case

The first validation case is the Turek benchmark case. The Turek benchmark case (Turek, 2006) is a well-known FSI benchmark case. It is mostly used for validation purposes and is therefore considered for the present study to validate the use of the IQN-ILS method on a strongly coupled problem.

4.1.1 Case description

The Turek case consists of a two-dimensional incompressible laminar flow around a fixed cylinder with an attached elastic flap. In this paper it is considered as a two-dimensional configuration with a parabolic inlet velocity with a no-slip condition at the wall. The considered computational domain is shown in Figure 4.1.

Several test cases are described in (Turek, 2006), however, for the present validation purpose

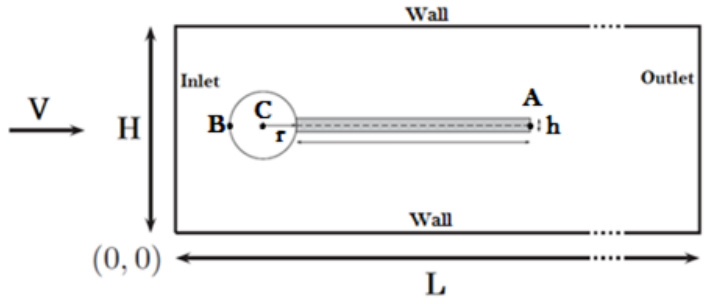

Figure 4.1: Geometry of the cylinder with attached flap of the Turek benchmark case. With r=0.05m, l=0.35m, h=0.02m, H=0.41m, L=2.5m and A is the reference point for the measured displacement. The solid domain is shown in gray and the fluid domain in white. Amended from (Turek, 2006)

parameter	FSI1	FSI2	FSI3
ϱ^s $[10^3 \frac{\text{kg}}{\text{m}^3}]$	1	10	1
ν^s	0.4	0.4	0.4
μ^s $[10^6 \frac{\text{kg}}{\text{ms}^2}]$	0.5	0.5	2.0
ϱ^f $[10^3 \frac{\text{kg}}{\text{m}^3}]$	1	1	1
ν^f $[10^{-3} \frac{\text{m}^2}{\text{s}}]$	1	1	1
$\bar{U}$ $[\frac{\text{m}}{\text{s}}]$	0.2	1	2
parameter	FSI1	FSI2	FSI3
$\beta = \frac{\varrho^s}{\varrho^f}$	1	10	1
ν^s	0.4	0.4	0.4
$\text{Ae} = \frac{E^s}{\varrho^f \bar{U}^2}$	3.5×10^4	1.4×10^3	1.4×10^3
$\text{Re} = \frac{\bar{U}d}{\nu^f}$	20	100	200
$\bar{U}$	0.2	1	2

Figure 4.2: Parameter settings for the full FSI benchmarks (Turek, 2006)

only the case FSI3 and FSI2 are used (see Figure 4.2). In FSI3 and FSI2 the velocity is such that the flap starts to oscillate, whereas in FSI1 the velocity is too low and the flap does not oscillate. In the FSI3 case the density ratio is small ($\rho_s/\rho_f = 1$) and in the FSI2 case the density ratio is larger ($\rho_s/\rho_f = 10$). Both cases, but specifically FSI3, have a low density ratio, and are therefore used to test the capability of the IQN-ILS algorithm to solve a strongly coupled system.

4.1.2 Simulation setup

For both the fluid and the solid domain, two different mesh sizes are considered, a coarse grid and a finer grid. The coarse grid, as partly shown in 4.3 has a mesh size of 5981 cells in the fluid domain and 82 cells in the structure domain. The finer grid, partly shown in Figure 4.4, has a mesh size of 23924 cells in the fluid domain and 328 cells in the structure domain. For both cases, and all domains a hexahedral mesh is used. The time step used in both the solid and the fluid part is 0.001 seconds. A second order backward scheme is used as the temporal

discretization scheme, see Table 4.1 and Table 4.2 for the other simulation settings.

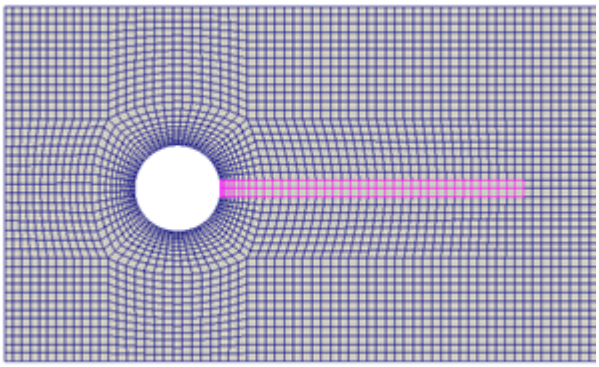

Figure 4.3: Small section of the coarse mesh, 5981 cells in the fluid domain (blue) and 82 in the structure domain (pink), used for the Turek benchmark case.

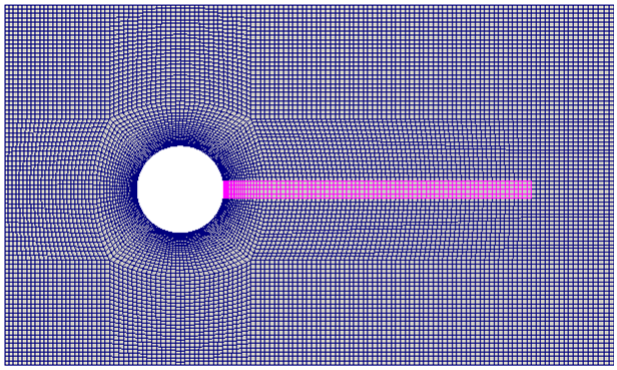

Figure 4.4: Small section of the fine mesh, 23924 cells in the fluid domain (blue) and 328 cells in the structure domain (pink), used for the Turek benchmark case.

Table 4.1: Simulation setup Turek fluid

	Scheme
Fluid solver	block-coupled transient incompressible flow solver
Solid solver	segregated solver
Interpolation	Radial Basis Function, thin plate spline
Up	BiCGStab with Cholesky preconditioner

Table 4.2: Simulation setup Turek solid

	Scheme
solid solver	elasticNonLinTLSolidFoam
gradient	Extended Least Squares
divσ	Gauss linear

4.1.3 Results and Discussion

The resulting displacement of point A (see Figure 4.1), and the drag and lift forces are shown in Figure 4.5, Figure 4.6 and Figure 4.7, Figure 4.8 respectively. The results of the FSI2 case are given after 34.0 up to 35.0 seconds (see Figure 4.5 and Figure 4.6), and for the FSI3 case the results are given after 19.5 up to 20 seconds (see Figure 4.7 and Figure 4.8) .

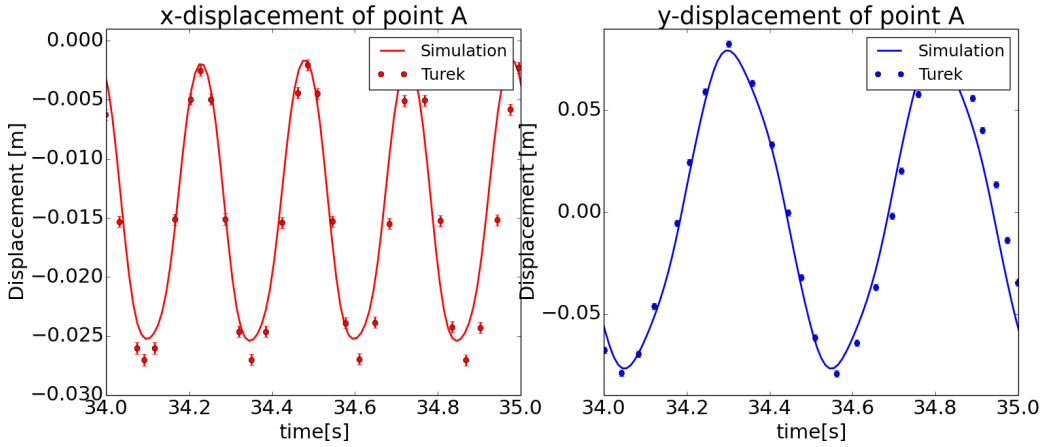

Figure 4.5: Displacement over time of point A with the numerical results presented in the Turek benchmark case FSI2 (Turek, 2006)

In both cases, the frequency of the oscillation is different from the oscillation frequency of the benchmark case. This difference is small but can be for example observed in the x-displacement plot of Figure 4.5. In this case the frequency in the simulation is approximately 3.86 Hz and the benchmark case has a frequency of approximately 4.0 Hz. This difference in frequency causes a phase shift after 34.0 seconds. The same effect can be observed in the displacement plot of Figure 4.7. In this case the frequency in the simulation is approximately 11.1 Hz and the benchmark case has a frequency of approximately 10.9 Hz. This difference in frequency causes a phase shift after 19.5 seconds. However, in order to make the comparison

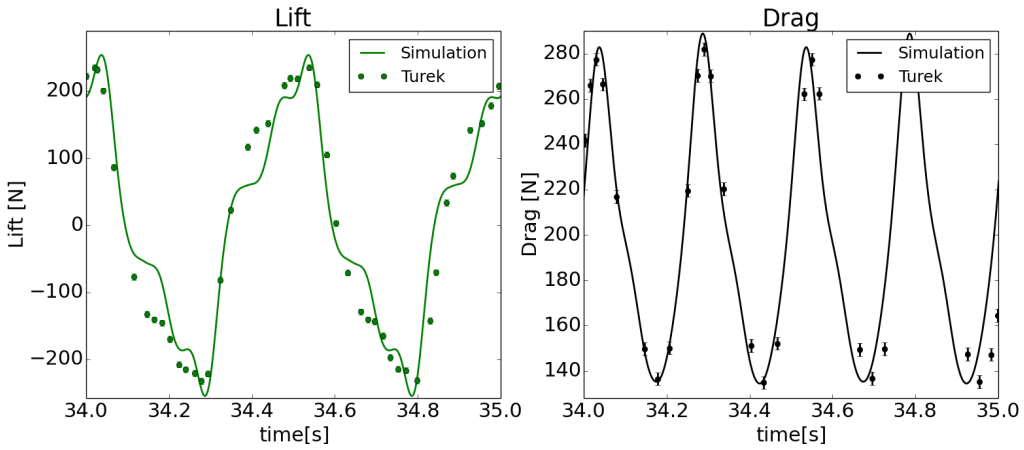

Figure 4.6: Displacement over time of point A with a coarse mesh and the numerical results presented in the Turek benchmark case FSI2 (Turek, 2006)

between the simulation and the Turek benchmark data easier, this phase shift is removed in Figure 4.5, Figure 4.6, Figure 4.7 and Figure 4.8.

Table 4.3: Amplitude and mean of the x-displacement, y-displacement, drag and lift for the simulation and the Turek FSI2 benchmark case (Turek, 2006)

Sim	x-displacement [m][10^{-3}]		y-displacement [m][10^{-3}]		Drag [N]		Lift [N]	
	Mean	Amplitude	Mean	Amplitude	Mean	Amp.	Mean	Amp.
Coarse	-14.51	10.9	1.05	78.41	196.81	92.04	3.29	250.86
Turek	-14.58	12.44	1.23	80.6	208.83	73.75	0.88	234.2

Figure 4.5 and Table 4.3 show that the x-displacement of point A is underestimated. However, the amplitude of the lift and drag (see Figure 4.6) are higher compared to reference, see also Table 4.3.

Table 4.4: Amplitude and mean of the x-displacement, y-displacement, drag and lift for the simulation and the Turek FSI3 benchmark case (Turek, 2006)

Sim	x-displacement [m][10^{-3}]		y-displacement [m][10^{-3}]		Drag [N]		Lift [N]	
	Mean	Amplitude	Mean	Amplitude	Mean	Amp.	Mean	Amp.
Coarse	-1.96	1.84	3.97	26.01	444.62	20.40	-11.74	213.37
Fine	-1.62	1.72	1.93	26.7	457.26	26.32	-7.91	200.61
Turek	-2.69	2.53	1.48	34.38	457.3	22.66	2.22	179.78

Figure 4.7 and Table 4.4 show that the displacement of point A is underestimated for both the fine and the coarse grid. The obtained results for the lift and the drag forces are shown in Figure 4.8 and Table 4.4. From this it can be found that the lift and the drag forces are slightly overestimated. When refining the mesh, the amplitude of the lift and drag forces are decreasing, as a result the amplitude of the displacement is slightly decreased.

As is also found in section 4.2, the decreased amplitude is caused by artificial damping intro-

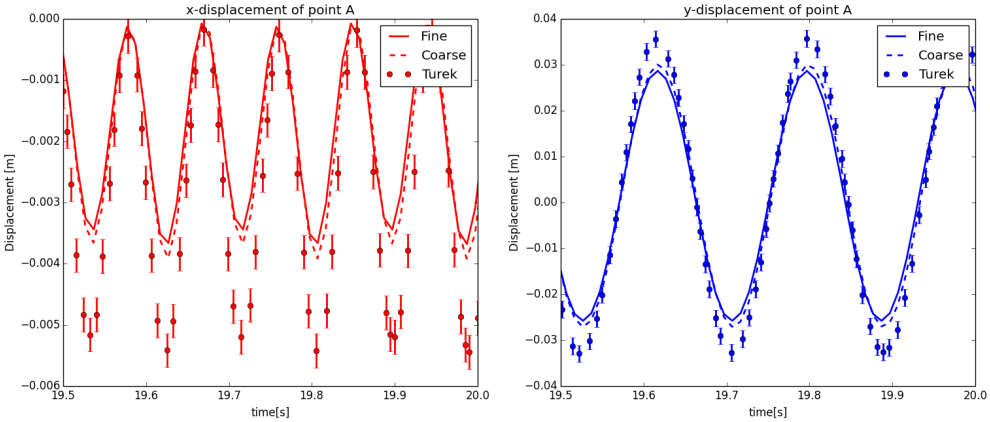

Figure 4.7: Displacement over time of point A for a coarse grid, a finer grid and the numerical results presented in the Turek benchmark case FSI3 (Turek, 2006)

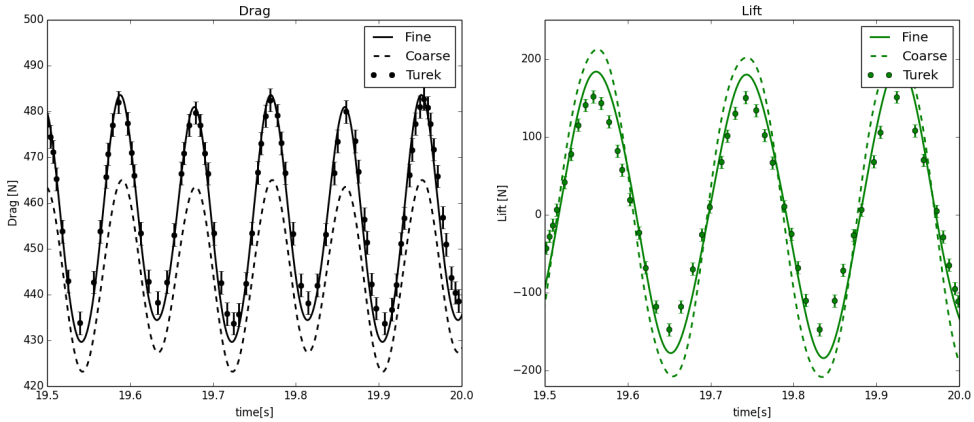

Figure 4.8: Displacement over time of point A for a coarse grid, a finer grid and the numerical results presented in the Turek benchmark case FSI3 (Turek, 2006)

duced by the temporal discretization method. As with the phase shift, the artificial damping is also summing up after 19.5 seconds, introducing an underestimation in amplitude. In this case the time step is fixed at 0.001 seconds.

When comparing the grid convergence it can be seen that for FSI2 a higher accuracy is obtained compared to FSI3. FSI2 has a lower fluid velocity and a lower oscillation frequency compared to FSI3 (approximately 4 Hz for FSI2 and 11 Hz for FSI3). Because of the lower velocity, the shear and boundary layer in the case of FSI3 are thinner compared to FSI2, which will be better resolved when using a finer grid. In this section is it shown that the IQN-ILS method can be used to solve for strongly coupled problems.

4.2 Vattenfall free vibration case

Vattenfall Research and Development in Sweden has performed an experiment (Vu and Truc, 2014) where a vertical slender rod with a roller boundary condition and a clamped side is displaced and then released. After which its vibrations and damping under the influence of the surrounding fluid are investigated.

4.2.1 Experimental setup

The slender rod, or the bar is located inside the perspex channel. Water or air is pumped in longitudinal direction of the beam trough the perspex channel. The centre of the rod is given an initial displacement of 10 mm after which it is released, after which it can freely vibrate. The displacement of the rod is measured using a laser, the laser is located at 835 mm measured from the bottom of the rod. All results shown in this section are measured at this location.

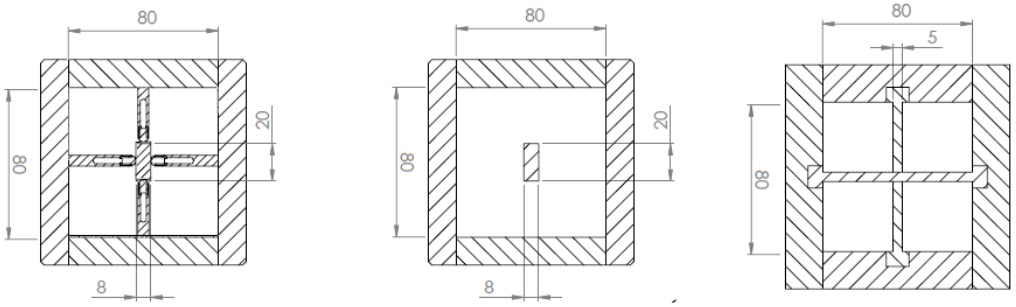

(a) Top of rod, 'roller' boundary condition

(b) Rod at half length, free

(c) Bottom of rod, clamped boundary condition

Figure 4.9: Construction drawings of the boundary conditions of the Vattenfall experiment

Figure 4.9 shows the cross-section of the test section at the top, center and bottom location. The bottom the rod is clamped and the top of the rod is clamped in the all directions except for the beam longitudinal direction.

Table 4.5: Water flow velocities and temperatures measured during experiment

Velocity [m/s]	Temperature [$^{\circ}C$]
0	13.6
1	8.4
3	11.6

Measurements in quiescent air and water were performed initially, subsequently tests in water with a flow rate of 1.0 m/s and 3.0 m/s in the axial direction were performed. This case can therefore be used to test the influence of the added mass. The rod has a length of $L = 1.5$ m, the material of the rod is stainless steel, with a density of $\rho = 8000\,\mathrm{g}\,/\,\mathrm{cm}^3$, a modulus

of elasticity of $E = 193\,\text{GPa}$ and the moment of inertia is $I = 8.53 \cdot 10^{-10}\,\text{m}^4$. For the test performed with air the temperature was 17.7° C and the pressure 1012.7 hPa. When water was used the temperatures where varying more, see Table 4.5.

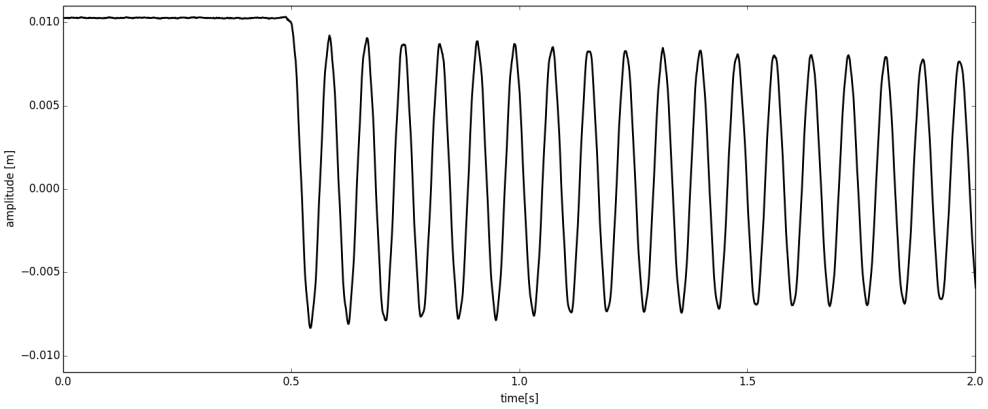

Figure 4.10: Experiment measurement at h=835 mm, quiescent air

The first experiment, measuring the displacement of the beam is performed in quiescent air, in all experiments the laser measured the displacement of the beam at a hight of 835 mm from the ground. The added mass of air is relatively small and can be therefore neglected in this case. Figure 4.10 shows the measured displacement. As can be seen here the beam is deflected until (approximately) 10 mm after which it is released and can freely vibrate. The frequency of this vibration is approximately 12.3 Hz.

When solving the case analytically, the frequency of a clamped-roller supported beam can be calculated with (Rajesekaran, 2009):

$$\omega = \frac{15.418}{L^2}\sqrt{\frac{EI}{\rho A}}, \tag{4.1}$$

with ω being the natural frequency and, L the beams length, E the modulus of elasticity, I the moment of inertia, ρ the density of the material and A the area. The analytic approximation of the beams frequency results in 12.37 Hz, this is very close to the value of 12.3 Hz measured in the experiment.

Figure 4.10 shows also a decreasing oscillation amplitude over time. This is induced by the forces exerted by the fluid on the structure, but also due to the solid damping.

Damping ratio

When considering a coupled FSI case, the source of the damping can be the fluid or the structure. When considering the damping of the structure it can be the material damping or the friction at the supports. In the experimental case the friction at the supports is not strictly known, in theory the solid can slide freely in its longitudinal direction, however this can be slightly different in the experiment. In the simulation material damping is assumed to be zero.

4.2.2 Simulation Setup

In this section the simulation setup is discussed. The considered computational domain is shown in Figure 4.11.

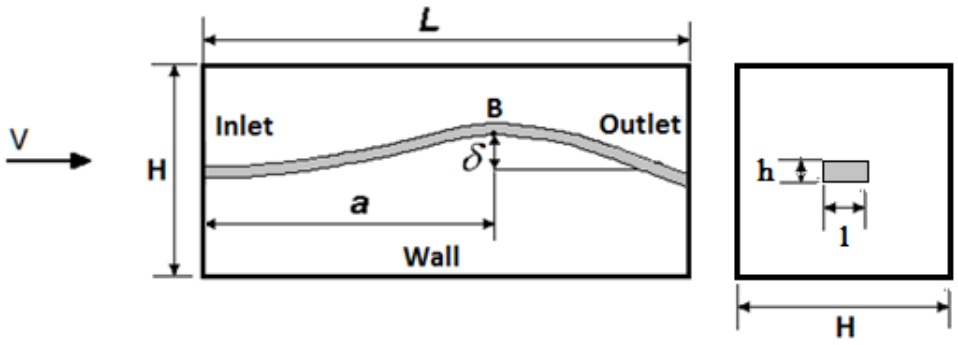

Figure 4.11: A schematic drawing of the Vattenfall experiment where L=1.5m, a=0.75m, H=0.8m, h=0.008m, l=0.02m and the initial displacement = 0.01 m. The gray represents the solid domain and the white the fluid domain

Solid Figure 4.12 shows the mesh for the solid domain. For this relatively simple geometry a hexahedral mesh is chosen, this is optimal since it will result in the smallest amount of cells for a given base-mesh size. On the length of the beam the mesh is split into two sections with length $x1 = 0.75$ m. On the left side of the beam (point A of Figure 4.12) a patch is located where the fixed boundary condition is applied. A small patch of 1 mm is located at the bottom centre of the beam (in point B of Figure 4.12) , this is used to apply the initial displacement at the center of the beam. At the end of the beam, so at the right bottom and top (point C of Figure 4.12) side of the beam, another small mesh patch (0.1 mm) is located. These patches are created to be able to set the boundary conditions in OpenFOAM at these positions, no changes are made to the actual geometry.

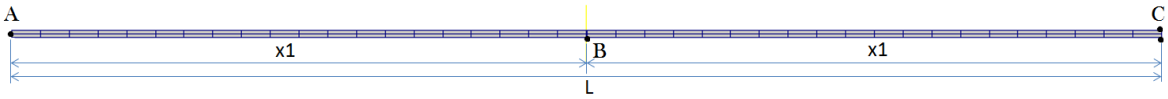

Figure 4.12: Solid mesh, $L = 1.5$ m and $x1 \approx 0.750$ m

In the calculations three different boundary conditions were used to simulate the 'roller' boundary condition as can be seen in Figure 4.9. The three different boundary conditions are called 'single roller support' (SRS), 'double side roller support' (DSRS), 'longitudinal free' (LF). This was necessary because it was not clear how the boundary condition of the experiment could be reproduced in the simulation. The 'single roller support' and 'two side roller support' both use the boundary condition 'fixedDisplacementZeroShear' of OpenFOAM whereas 'single roller support' only uses this condition on a small patch at the bottom. The 'two side roller support' has a patch on all sides, which is more like the experimental boundary condition shown in Figure 4.9. The third boundary condition 'longitudinal free' uses the mixed boundary condition of OpenFOAM on the top patch of the rod. This boundary condition applies a zero force on the normal of the patch while the shear directions are fixed. This boundary condition was used as a first attempt, since the description of the boundary condition on the roller side of the beam was that it the beam should be able to move freely in its longitudinal direction (so the patch normal) and be fixed in the other directions.

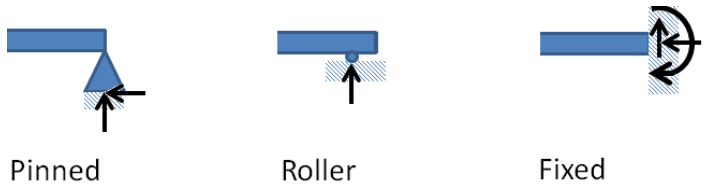

Figure 4.13: Different kind of boundary types and their reaction forces

Figure 4.13 shows the difference in boundary conditions and reaction forces. When using a different boundary condition the stiffness of the system changes and will therefore result in a different oscillation frequency.

In the experiment the centre of the beam is displaced 10 mm using a wire, before it is released, after which it can freely vibrate. In the simulation a patch at the center of the beam is created where the initial displacement is applied using the 'fixedDisplacementZeroShear' boundary condition in OpenFOAM. The initial displacement, stresses and strains can than be mapped onto the case where the beam can freely vibrate. The settings for the solid solver can be found in Table 4.6.

Fluid The settings for the fluid solver can be found in Table 4.7 and 4.8 . A snap shot of the undeformed fluid mesh is given in Figure 4.14.

Table 4.6: Simulation setup Vattenfall solid only

	Scheme
solid solver	elasticNonLinTLSolidFoam
$\frac{\partial^2}{\partial t^2}$	Euler (first order implicit) / second order backward (second order implicit)
gradient	Extended Least Squares
divσ	Gauss linear

Table 4.7: Solvers Vattenfall fluid and coupling

	Scheme
Fluid solver	block-coupled transient incompressible flow solver
Up	BiCGStab with Cholesky preconditioner
Solid solver	segregated solver
U	PCG with DIC preconditioner
Interpolation	Radial Basis Function, thin plate spline

Table 4.8: Fluid Schemes

Variable	Scheme
ddtSchemes	bdf2
gradSchemes	Gauss linear
divSchemes	
div(pi,U)	Gauss skewCorrected linear
div((nuEff*dev(grad(U).T()))	Gauss linear
div(U)	Gauss linear
laplacianSchemes	skewCorrected linear
snGradSchemes	corrected

(a) Front view

(b) Side view

Figure 4.14: Undeformed fluid mesh, front view, mesh shown here contains approximately 6272 cells

Coupling Since, the mass ratio of the experimental case is $\rho_f/\rho_s = 8$ (using water as the fluid medium), which is larger compared to the Turek benchmark case (even larger when the fluid is air). The IQN-ILS coupling algorithm is chosen for this case, because in section 4.1 it is shown that this method works well for comparable or even lower mass ratios. It is therefore expected that it will also perform well for this case.

4.2.3 Results and Discussion

First only the solid solver of OpenFOAM was used to check the influence of the mesh, the timestep and the boundary conditions.

Solid

In this section only the solid solver of OpenFOAM is used. The mesh convergence study is performed for the three different boundary conditions 'single roller support', 'two side roller support', and 'longitudinal free'.

Influence of grid size First the influence of the mesh is checked using a small time step (Δt=0.00001 s). The obtained results can be found in Figure 4.15.

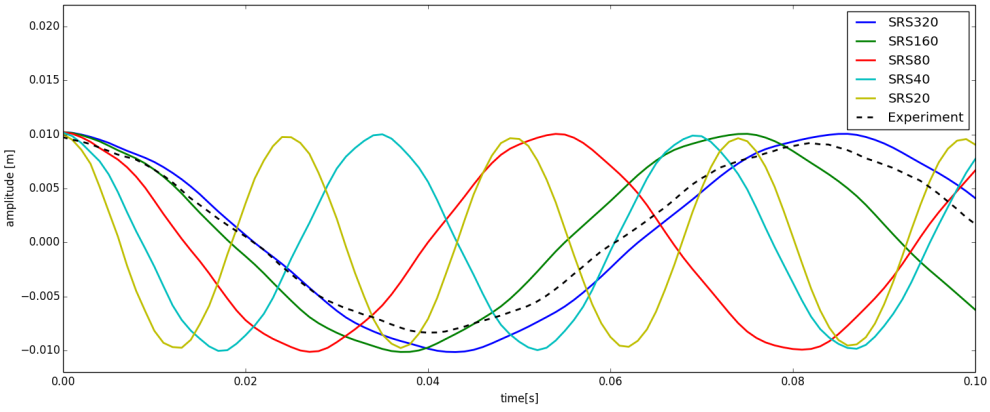

Figure 4.15: Grid convergence study Δ t=0.00001 s, boundary condition single roller support(SRS). Where SRS20, SRS40, SRS80, SRS160, and SRS320 have respectively 20, 40, 80, 160, and 320 cells in the x1 direction

Figure 4.15 shows the grid convergence study performed with the SRS boundary condition. The grid convergence study was performed using a 2D geometry with 20, 40, 80, 160 and 320 cells in x1 (see Figure 4.12) direction 3 cells in the y direction. From this it can be seen that the mesh has a large influence on the oscillation frequency.

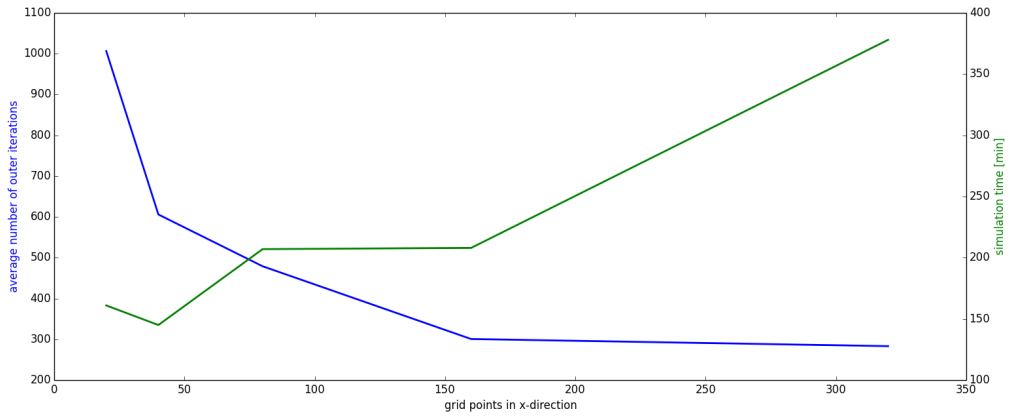

Figure 4.16: Grid convergence study Δt=0.00001 s, time and number of iterations for the SRS boundary condition

Figure 4.16 shows the number of outer iterations iterations and the simulation time for different mesh refinements. Combining this together with the results shown in Figure 4.15, it can be seen that when using a too coarse mesh (20 cells in x1 direction) both the accuracy and the runtime are worse compared to for example the mesh with 40 cells in x1 direction. Increasing the number of cells in x1 direction will decrease the average number of outer iterations, which means that the structure solver can converge more easily. However, when using a finer mesh, the simulation time also increases.

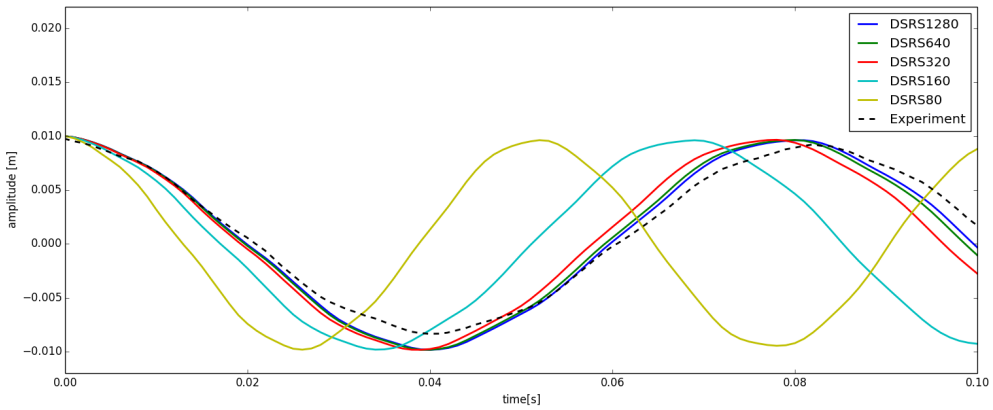

Figure 4.17: Grid convergence study Δt=0.00001 s, boundary condition double sided roller support(DSRS). Where DSRS80, DSRS160, DSRS320, DSRS640, and DSRS1280 have respectively 80, 160, 640, and 1280 cells in the x1 direction

Also for the DSRS boundary condition a grid convergence study was done. Figure 4.17 shows that when decreasing the grid in x1 direction to 320 cells the difference becomes small.

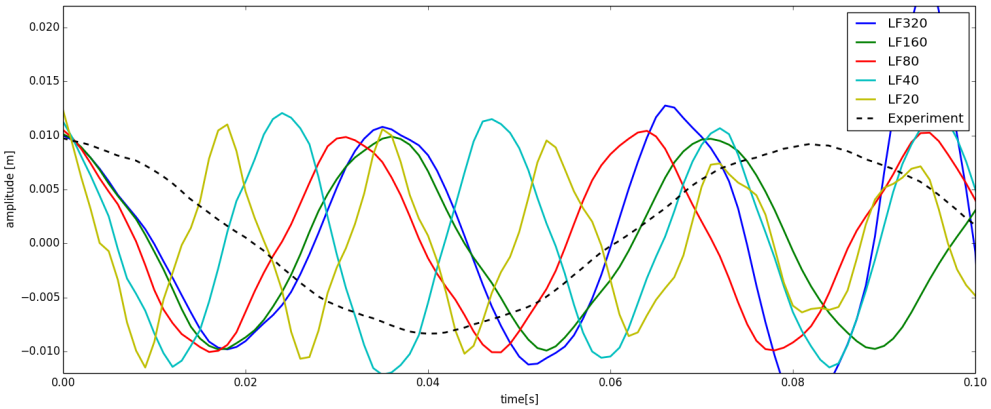

Figure 4.18: Grid convergence study Δt=0.00001, boundary condition longitudinal free. Where LF20, LF40, LF80, LF160, and LF320 have respectively 20, 40, 80, 160, and 320 cells in the x1 direction

The impact of going from 2D to 3D simulation is shown in Figure 4.19. It can be seen that the frequency using the 2D case is slightly overestimated. The effect relatively to the increas of the mesh size, is however less compared to refining in the x1 direction.

Table 4.9: Oscillation frequencies of the double sided boundary condition

Case	Number of cells	Frequency [Hz]	error %
Experiment	-	12.3	-
DRSR80	486	20.16	63.9
DRSR160	966	15.96	29.76
DRSR160 3D	2898	15.13	23.01
DRSR320	1926	13.45	9.35
DRSR640	3846	12.71	3.33
DRSR640 3D	11538	12.32	1.3
DRSR1280	7686	12.71	3.33

Table 4.9 gives an overview in the measured frequencies. From this it can be also seen that when refining the mesh in x1 direction the error decreases more compared to going from 2D to 3D. The number of cells however increases drastically for the 3D case.

Also for the LF boundary condition a mesh convergence study was performed. As can be seen in Figure 4.18 this boundary condition behaves in a strange way.

From Figure 4.20 it can be seen that the different boundary conditions on the right hand side of the beam causes the total beam to deform differently, which also results in a different stress and strain levels in the beams. This causes the beam to behave differently when released. In case of the LF boundary condition (red), the beam did not move inwards at the right boundary and seems to be longer at this point compared to the undeformed state. This is not the case in the experiment, and should not be the case since the 'roller' boundary

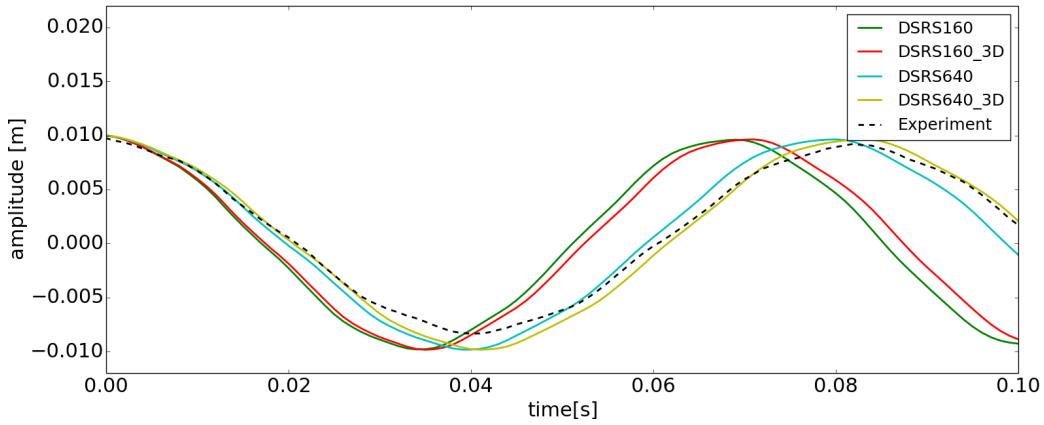

Figure 4.19: Grid convergence study Δt=0.00001 s, boundary condition double sided roller support. Where DSRS160 and DSRS640 are the 2D solids, and 3D denotes the 3D the solids.

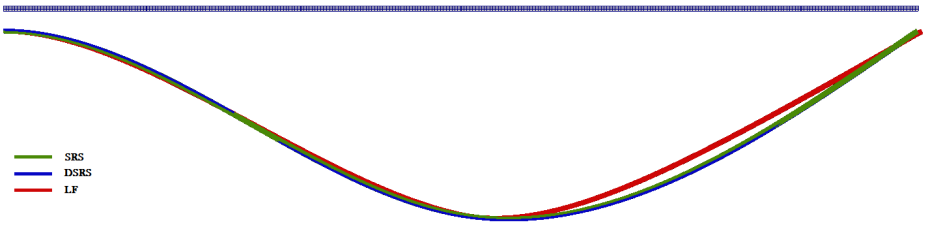

Figure 4.20: Top part of figure shows undeformed solid. Bottom part shows the initial displacement of the solid (magnitude of displacement is multiplied by 30) for the three different boundary conditions SRS (green) ,DSRS (blue) and LF(red)

condition should allow for longitudinal movement. This boundary condition therefore causes non physical behaviour, and will not be further used in this study.

Influence of time discretization In this section the influence of the time step on the solution is evaluated. Figure 4.21 shows the influence of of the timestep on the damping. Since no damping coefficient is used in the OpenFOAM the oscillation should not dampen. The decrease in amplitude is therefore caused by artificial damping introduced by the temporal discretization method. Since such a strong effect of the timestep is observed, instead of the Euler time discretization scheme a second order backward scheme is used.

However changing from the Euler time discretization scheme to a second order backward scheme did not have the expected effect. Figure 4.22 shows the Root Mean Squared (RMS) error calculated using the results obtained with $\Delta t = 0.00001$ as a reference. When comparing the second order backward scheme (bdf2) with the first order Euler scheme, it can be observed that bdf2 has a smaller error with the same time step. However one would expect a second order scheme to have a second order decrease of error while only a first order (linear) behaviour

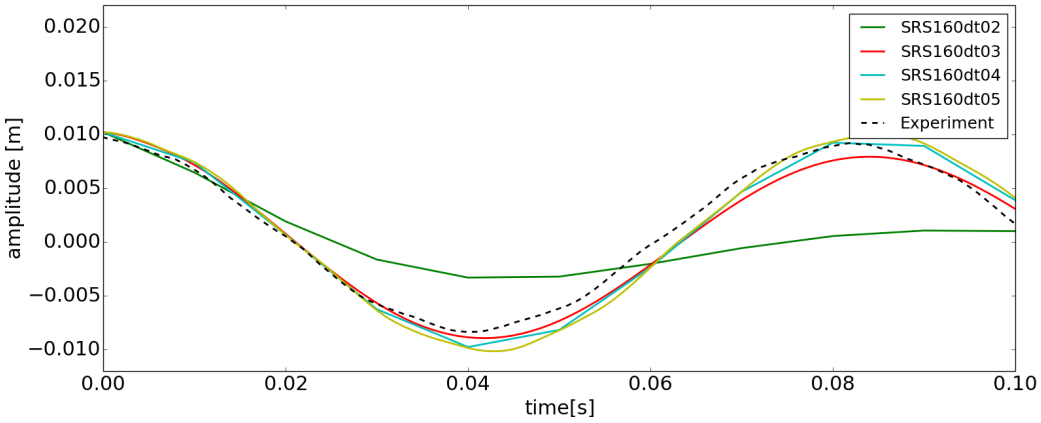

Figure 4.21: Resulting displacement of point B of five different simulations and Vattenfall experiment in air at V=0m/s. In this the Euler discretization scheme is used. All simulations use a grid spacing of 160 in x1 direction, the single roller support and a Δt between $0.01 - 0.00001$ (respectively dt2-dt5)

is observed.

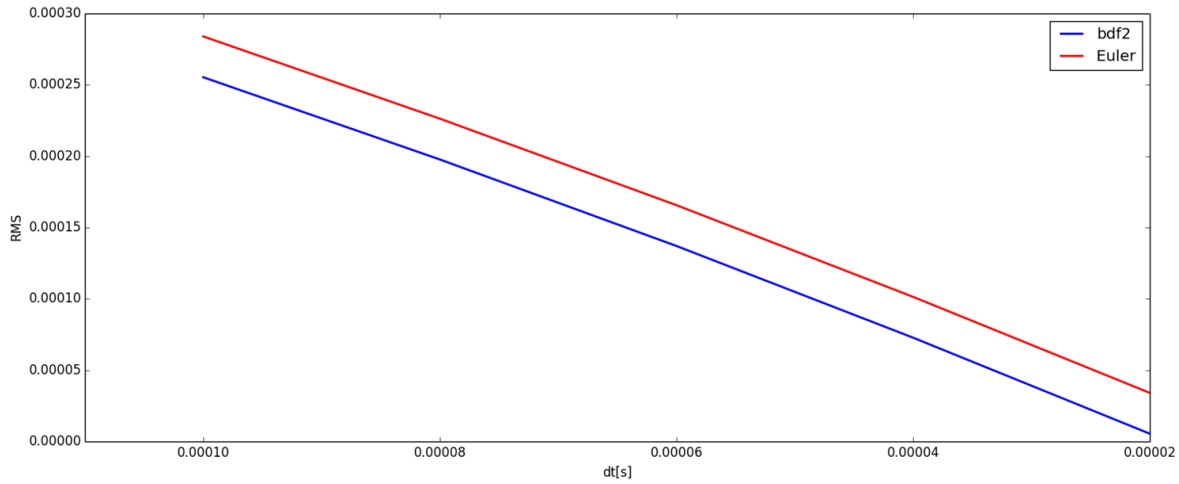

Figure 4.22: RMS of different time discretization schemes Euler and second order backward (bdf2)

Coupled fluid and structure

In this section the results of the coupled case are given. First an attempt was made to solve the domain in 2D. However since the fluid is considered to be incompressible and with the solid vibrating, the fluid was not able to adjust to the motion of the beam since it was not able to flow around the beam. Therefore all the following cases are performed in a 3D domain.

The grid size of both the solid and the fluid domain is the same for all cases (air 0 m/s, water 0 m/s, water 1m/s, and water 3m/s) unless noted otherwise, with 11538 cells in the solid and 7212 cells in the fluid and Δt=0.0001 s. Since the initial condition of the solid is a deformed state, also the fluid mesh has to be deformed to match the solid region. A utility *'mapMesh'* was created in OpenFOAM to displace the fluid mesh when imposing the initial displacement of the solid. A snapshot of the initial mesh and displaced solid can be found in Figure 4.23

Figure 4.23: Deformed fluid and solid mesh

The first case is the solid coupled with the quiescent air. The resulting displacement of the solid can be found in Figure 4.24. This case was run with two different meshes, 20 and 160 cells in x1 direction.

In the case of the coarse mesh, a difference can be still observed between SRS20c and SRS20,

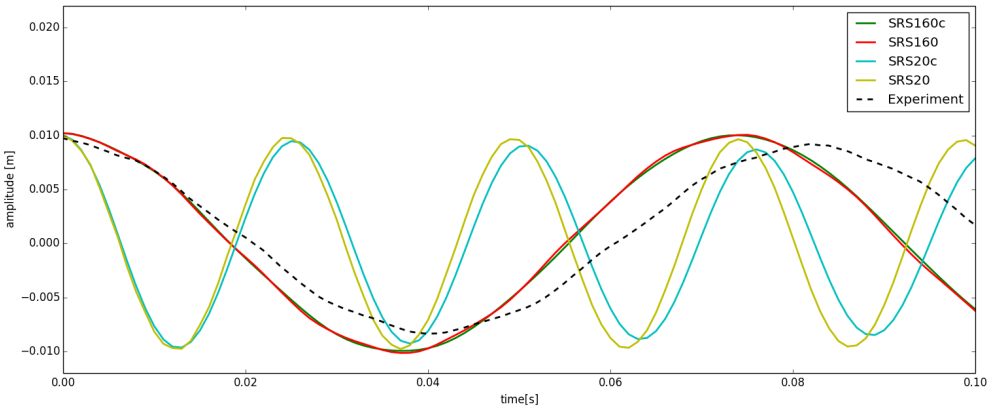

Figure 4.24: Oscillation of solid, air V=0 m/s, with different meshes refinements, and for boundary condition SRS. Where SRS160c and SRS20c are the coupled simulations and SRS160 and SRS20 are the solid only simulations.

this damping is mainly caused by the numerical damping as Δt =0.0001 s in the coupled case. Since the added mass in the case of air is low, its influence on the solid is low. This is also observed in the finer case, where the results of the coupled case lies on top of the results obtained with only the solid solver.

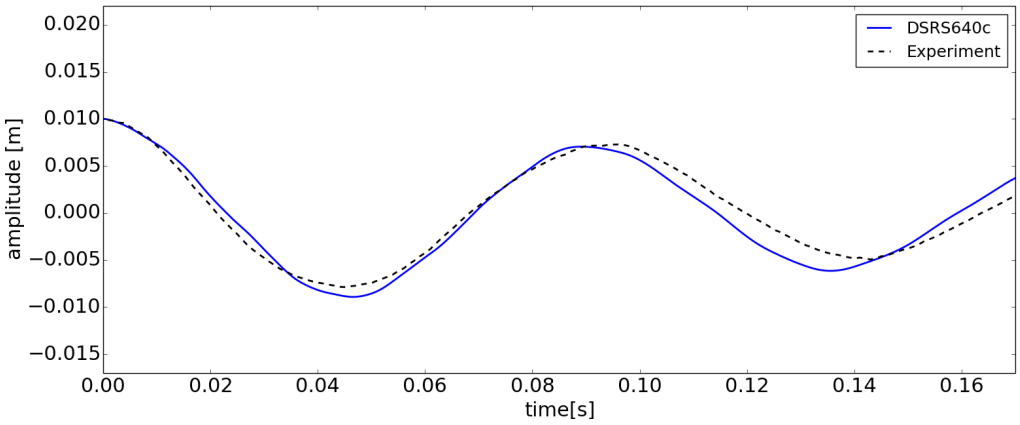

Figure 4.25: Displacement solid, water 0 m/s

The second coupled case is the solid coupled with quiescent water. The resulting displacement of the solid can be found in Figure 4.25. These results can be used to get the influence of the added mass. The change in frequency between the solid only and the water 0 m/s gives an indication of the effect of the added mass. Since in this case the wall is placed at a relatively large distance from the vibrating beam, confinement parameter χ is one (Chen, 1985). It can

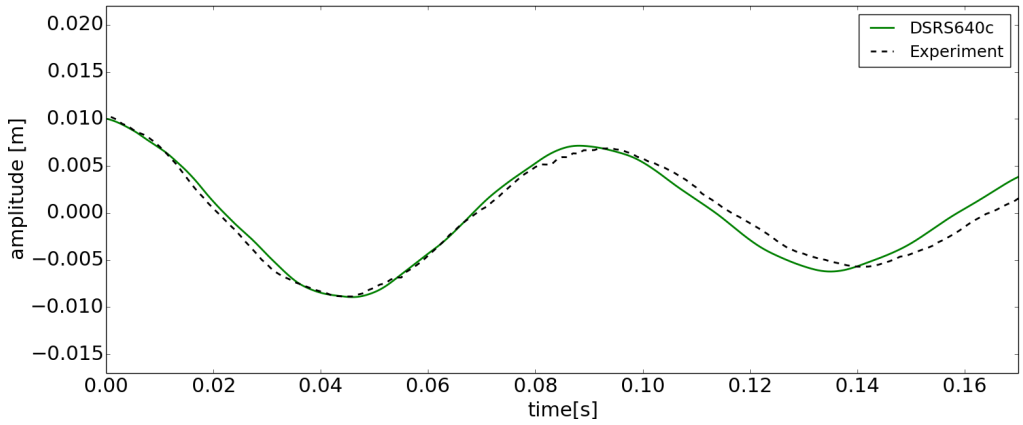

Figure 4.26: Displacement solid, water 1 m/s

be found that analytically the change in frequency should be

$$\omega = \frac{15.418}{L^2}\sqrt{\frac{EI}{(\rho_s + \rho_f)A}}, \tag{4.2}$$

with ω being the natural frequency and, L the beams length, E the modulus of elasticity, I the moment of inertia, ρ_s the density of the solid, ρ_f the density of the fluid and A the area. This results in a frequency of 11.66 Hz. The frequency of the experiment for water at 0 m/s is 10.57 Hz, while the simulation resulted in 10.61 Hz. The analytical calculation of the added mass underestimates the influence of the added mass, while the simulation frequency is close to that of the experiment. The error between the simulation and the experiment is in the same order as the error obtained with the mesh convergence study, see Table 4.9.

The third coupled case is the solid coupled with water at V=1 m/s. The resulting displacement of the solid can be found in Figure 4.26

The fourth coupled case is the solid coupled with with water at V=1 m/s. The resulting displacement of the solid can be found in Figure 4.27

Only a small difference in frequency of the simulation with respect to the experiment is observed. When comparing this to the error made using only the solid solver with this amount of cells, this difference is mainly caused by the error made by the solid solver.

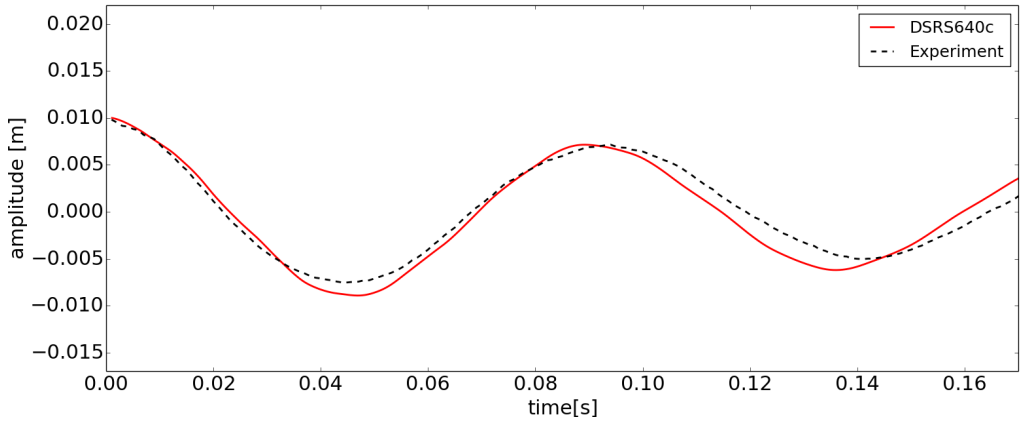

Figure 4.27: Displacement solid, water 3 m/s

4.3 Summary

A validation study is performed in this chapter. The coupling method IQN-ILS is used to solve two strongly coupled cases with a low density ratio. The first case is the Turek numerical benchmark case, from this it was found that the IQN-ILS method is able to handle strongly coupled problems. In the second case, the Vattenfall experiment it was found that the time step, the mesh size and the boundary condition have big influence on the frequency and damping of the vibration. It was also found that when the fluid and solid solvers are coupled using the IQN-ILS method the amplitude and frequency of the vibration are similar to the experimental values. So the influence of the fluid on the solid, the influence of the added mass, was modelled correctly using the IQN-ILS method.

Chapter 5

Industrial application

After validating the use of the IQN-ILS coupling method in the previous chapter, this chapter applies the used method on a geometry that is closer to the real application. This is a test case based on the fluid flows and structures found inside the core of a nuclear power plant. In this particular case the geometry is equivalent to the neutron detector housing tube, also called ICI (see the destructive effect of FIV on ICI's in the Introduction chapter), found inside the reactor core, together with its surrounding fuel box corners and housing tube.

5.1 Experimental setup

This experiment is also performed by Vattenfall Sweden, but to avoid confusion with the Vattenfall case from section 4.2, this case is referred to as the industrial application. A schematic drawing of the core fuel boxes and detector guide tube position, and the dimensions of the detector guide tube can be found in Figure 5.1.

The bottom of the guide tube is fixed in the core support plate and the upper end is fastened in the core grid with a spring. The fundamental frequency of such a system is in the range of 2-3 Hz. For a large boiling water reactor (BWR) the bypass flow is as large as 1000-1800 kg/s divided into 125-169 channels, one for each super cell (four fuel bundles) in the core. With an average density ρ=762 kg/m^3 at a temperature of T=286 °C the resulting average flow velocity is in the range of 2 m/s.

Since the same test section was used as in section 4.2, the experiment had to be scaled. This is done by keeping the fundamental frequency of system system constant. Since the ratio of the length of test section to the length of a real guide tube is 0.37, the wall thickness of the

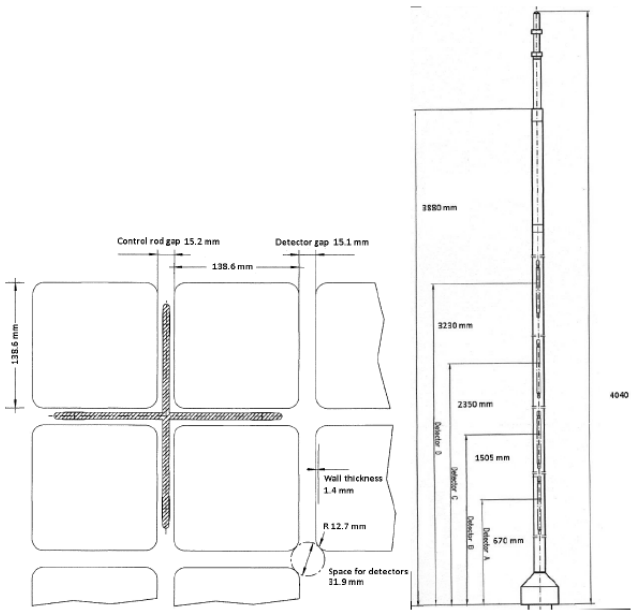

Figure 5.1: Schematic representation of the boxes surrounding the fuel rods and the detector guide tube position (left), with the detector guide tube dimensions (right).

beam has to be decreased to keep the frequency constant with

$$\omega = \frac{C}{L^2}\sqrt{\frac{EI}{\rho_s}}, \tag{5.1}$$

where E is the Youngs modulus, L is the tube length, $I = \frac{\pi}{4}(r_{outer}^4 - r_{inner}^4)$, the area moment of inertia, with r_{inner} and r_{outer} being the inner and outer radius of the guiding tube. For fixed-pinned and fixed-free boundary conditions the constants are $C = 15.418$ and $C = 3.5156$ respectively. In this experiment a stainless steel tube with $r_{outer} = 4$ mm, $r_{inner} = 3.4$ mm, E= 214 GPa, $\rho = 7863$ kg/m^3, $\rho_s = 0.11$ kg/m and $L = 1.486$ m. Using this the fundamental frequencies of the fixed-free and fixed-pinned boundary conditions are 3.5 Hz and 15.2 Hz.

The supplied data are pressure measurements, velocity measurements, and solid displacement. The pressure measurements are performed using pressure transducers where the differential pressure transducers used have a range of 100 mbar, an uncertainty smaller than $\pm 0.5\%$ FSO (corresponding to 0.5 mbar) and a response time $\leq$ 5 ms. The velocity is measured using electromagnetic mass flow measurements. The vibration, or displacement, of the beam is measured using two high speed cameras with Particle Tracing Velocimetry. Table 5.1 shows the locations of the pressure and displacement measurements.

Three different experiments where performed. One with a fluid (water) flow of 15 l/s, 10 l/s

Table 5.1: Measurement locations of the pressure in the fluid domain and displacement of the solid

Location (x y z) [mm]	What is measured
(4.781,-4.781,1300)	p, displacement
(4.781,-4.781,1300)	p, displacement
(4.781,-4.781,1300)	p, displacement
(4.781,-4.781,1300)	p, displacement
(3.2,-13.6,1300)	p
(3.2,-13.6,1300)	p
(3.2,-13.6,1300)	p
(3.2,-13.6,1300)	p

Table 5.2: Properties experiment

Property	Value
Rod length (between BCs)	1.486 m
Rod diameter	0.008 m
Rod wall thickness	0.0006 m
Rod density	7863 kg/m3
Youngs modulus	214 GPa
Water density	998 kg/m3
Temperature	20 C
Rod upstream support	Fixed
Rod downstream support	Pinned
Boundary layer	Not tripped
Inflow boundary	Flowrate 0-15 l/s
Outflow boundary	Fixed pressure

and 5 l/s. Table 5.2 gives an overview of the properties of the experimental setup.

5.2 Simulation setup

Since in this case the fluid is forcing the solid, it is really important that the turbulence of the flow is modelled correctly. The geometry of the computational domain is given in Figure 5.2.

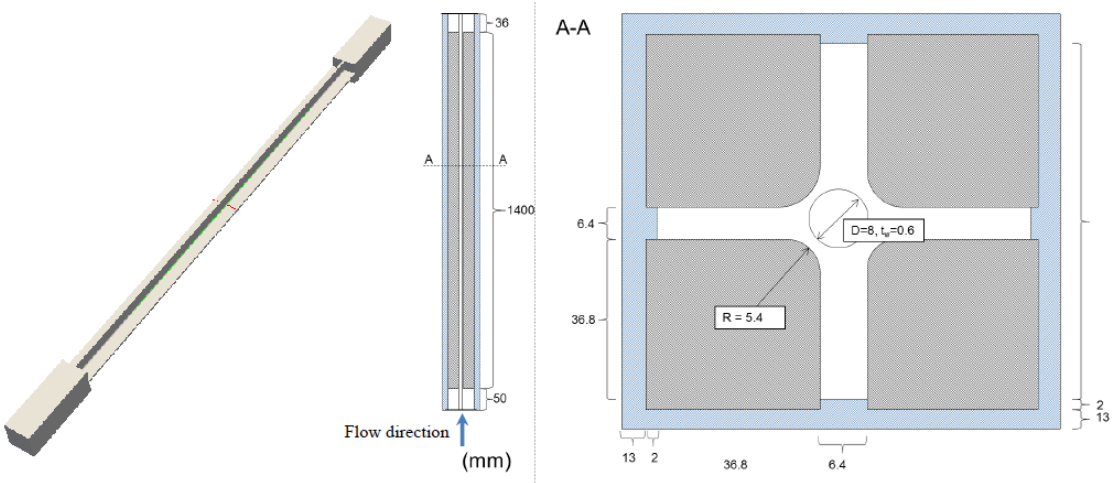

Figure 5.2: Fluid domain for the industrial application

5.2.1 Fluid

For the current application the modelling of the flow becomes more important, compared to the previous validation cases. From the experiment it is found that in this case the source of the flow induced vibrations is turbulence. From the most well known methods, LES is chosen as turbulence modelling approach for the current application, see section 3.10.

Adequate spatial resolution is a critical factor in the successful application of LES. Often applied criteria for the mesh are the mesh spacing in wall units (Georgiadis et al., 2010):

$$50 \leq \Delta x^+ \leq 150 \tag{5.2}$$
$$\Delta y^+_{wall} < 1 \tag{5.3}$$
$$15 \leq \Delta z^+ \leq 50 \tag{5.4}$$

With the criteria $y^+_{wall} < 1$ and 5l/s as the inflow boundary condition, the hight of the first

cell can be calculated:

$$h_{cell} = 2y, \tag{5.5}$$

where

$$y = \frac{y^+ \nu}{u_\tau}, \tag{5.6}$$

where

$$u_\tau = \frac{\mathrm{Re}_\tau \nu}{D_{eq}} \tag{5.7}$$

where u_τ was approximated to be 0.4898 at the 10 m/s test case. From this it can be found that the maximum height of the first cell has to be $h_{cell} = 7.6096e - 06$ m, using the criteria $y^+_{wall} < 1$. Using a stretching ratio of 1.07 close to the wall, $\Delta y^+ = 15$, $\Delta x^+ = 150$ and $\Delta z^+ = 50$ will result in a mesh containing more than 30 million cells. The computational power necessary to solve and couple such a fine mesh is not available for the current project.

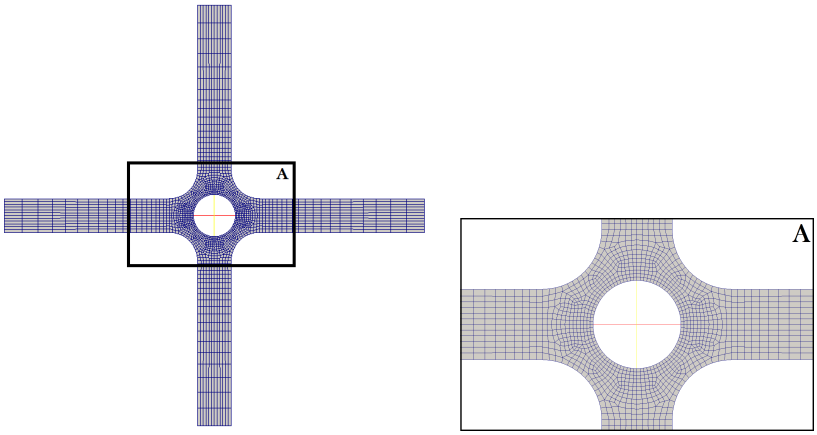

(a) Coarse fluid mesh

(b) Coarse fluid mesh (zoom of region A)

Figure 5.3: Coarse fluid mesh, total mesh size approximately 1.68 million cells

In the current case a coarser mesh is used, a snap shot of the mesh at the center of the domain can be found in Figure 5.3. When considering the 5 l/s case the wall y^+ value is equal to 70. It is therefore necessary to apply a wall function, see Table 5.3.

Table 5.3: Simulation setup industrial application fluid

	Scheme
Fluid solver	PISO
p	PCG with DIC preconditioner
U	PBiCG with DILU preconditioner
Solid solver	elasticNonLinTLSolidFoam
gradient	Extended Least Squares
divσ	Gauss linear
Interpolation	Radial Basis Function, thin plate spline

5.2.2 Solid

The boundary conditions of the solid are equal to the Vattenfall free vibration case, from section 5.4. Here it was found that the DSRS gives the best results and will therefore be applied in a similar way in this current case.

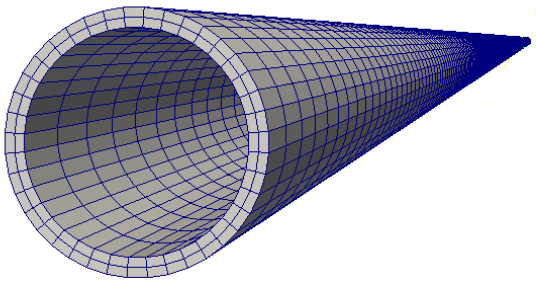

Figure 5.4: Solid mesh with 40080 cells

Figure 5.4 shows the mesh used for the solid. The total amount of cells in this mesh is 40080 (later referred to as S40080).

5.3 Results and Discussion

This section contains the results for the solid and the fluid, but the results for the coupled simulation are still pending.

5.3.1 Solid

Before coupling the fluid and the solid a mesh convergence study for the solid is performed. A distributed force (pressure) is given as an initial condition on the top of the solid. After this has converged the force is removed and the oscillation of the center of the beam is measured.

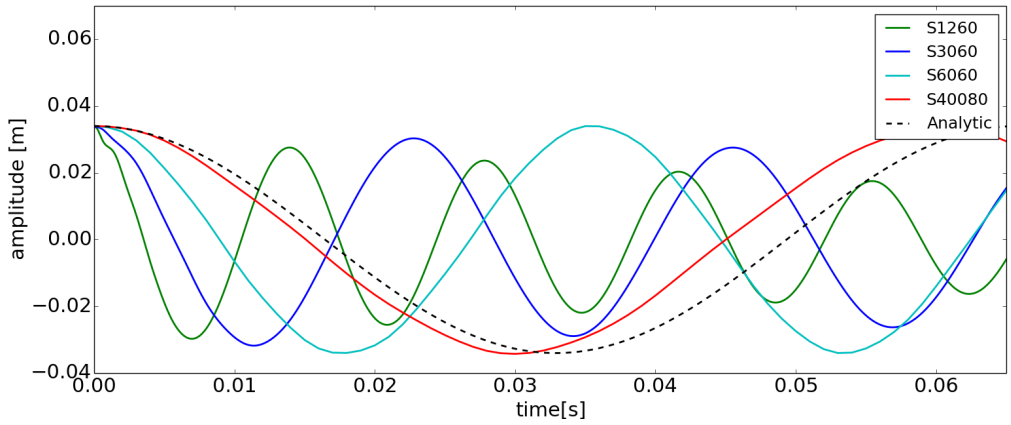

Figure 5.5: Grid convergence solid, with the DSRS boundary condition for a mesh with a total of 1260, 3060, 6060, and 40080 cells. The Analytic is just a cosine wave with the analytically calculated frequency of 15.2 Hz

Again the mesh of the solid domain has a big influence on the resulting frequency, as was also seen in section 4.2. Figure 5.5 shows the results for using the DSRS boundary condition. When increasing the grid, the oscillation of the beam converges towards the analytic solution of 15.2 Hz.

5.3.2 Fluid

In this section the results for only the fluid flow for the 10 l/s inflow condition are shown. In figure 5.6 it can be observed that the flow near the inlet is still laminar and has a low flow velocity (approximately 1.6 m/s). When the geometry becomes narrower the flow velocity increases, to a bulk velocity of 10 m/s and also becomes turbulent. However the pressure fluctuations of the flow in the simulation are in the order of 6 mPa while the pressure fluctuations found in the experiment are in the order of 60 mPa. Further research is therefore needed on the simulation of the turbulent flow.

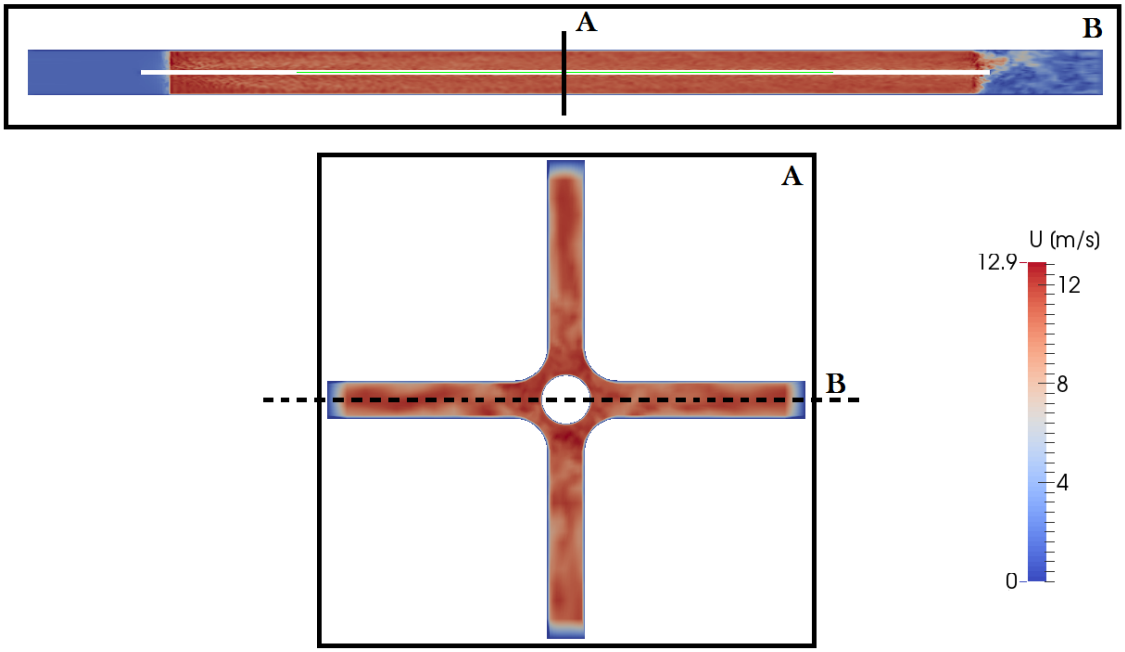

Figure 5.6: Fluid flow for the industrial application, 10 l/s inflow boundary condition

5.3.3 Coupled problem

In this case again the IQN-ILS method is used to couple the fluid and solid. The fluid and solid meshes are however much bigger compared to the cases shown in Chapter , which results in memory problems when coupling this case. It was found that when parallelization was applied, the memory usage increased even more. Therefore to be able to effectively use the previously applied methods on a industrial applications, this should be improved in the solver.

5.4 Summary

In this chapter the knowlege gained from the validation cases (Chapter) are applied. It is found that when refining the mesh for the solid the frequency of the first mode is correctly predicted and the boundary condition of the experiment is well represented in the simulation. Since the pressure fluctuations found in the flow only simulation are much lower compared to the experiment, further research is needed on the simulation of the turbulent flow. Also, while the fluid mesh is still coarse for a LES type case, all ready memory issues occur. Therefore to be able to handle industrial cases which require large amount of mesh points, the efficiency of the solver should be improved.

Chapter 6

Conclusions

In the framework of this Master Thesis, a numerical study of the FSI in nuclear reactor applications is performed. This is done using the tool OpenFOAM extended 3.1 combined with the FSI-FOAM solver. First a validation study was performed on the use of the IQN-ILS coupling method on a strongly coupled problem, this was done using the Turek benchmark case and the Vattenfall experiment. After this, the validated methods were applied on the industrial application to simulate the vibrations induced by the turbulent flow. The main research question of this project was *Are the currently available numerical simulation tools, fluid and structure solver with coupling algorithm, able to predict the onset of FIV in new reactor type applications?*

Using the Turek benchmark case it was proven that the IQN-ILS method is able to solve strongly coupled problems. When the velocities were higher, the mesh refinement had a bigger influence. Mainly because the shear and boundary layer have a big influence on the oscillation of the flap, and are not modelled correctly when taking a too coarse grid.

The second validation case, the Vattenfall experiment, showed that the IQN-ILS method can be also used to reproduce an experiment, and predict the added mass effect. This validation case also showed the influence of the mesh, the time step and the boundary condition on the resulting oscillation. It was shown that for this experimental setup, the Double Sided Roller Support (DSRS) gave the best results. When the time step was taken too large, numerical damping was added to the system which caused the damping ratio to be overestimated. When using a too coarse mesh for the solid, the stiffness of the beam was modelled incorrectly and therefore the frequency of the oscillation was overestimated. Because of the necessity for the solid to be refined, solving of the solid equations took more computational time compared to the solving the fluid equations. When a turbulent flow is simulated, the fluid mesh should be refined and therefore normally this is the other way around. However in this particular case solving the solid was the bottleneck.

The knowledge gained from the validation cases was then applied on the industrial application.

For the solid part, similar behaviour was shown when refining the mesh, when a too coarse mesh was used the frequency was overestimated. However, since in this case the vibrations are introduced by the turbulent flow another difficult modelling element was added. The large amount of cells needed for the modelling of the turbulent flow caused the fluid mesh to be big. Since the parallization of the FSI solver is not optimized, dividing the simulation over multiple processors gave memory issues.

To answer the research question, it is possible to predict the onset of FIV with the currently used simulation tool. The IQN-ILS coupling method works well for strongly coupled problems. Also the added mass is predicted correctly. The difference seen here is influenced by the solid mesh. There are however some parallelization problems and therefore the current implementation of the method is not fully suited for the industrial application, where large numbers of cells are common.

Chapter 7

Future Perspective

From the current work many things were found that could be done as future work. This chapter gives some suggestions for other test cases that can be performed. Also some further thoughts are given on the use of different modelling approaches.

7.1 Modelling

In the current study the IQN-ILS coupling method is used, there are however many other coupling methods. Could variations on the QN method, like the IQN-MVJ in (Lindner et al., 2015), have faster convergence? The Gauss-Seidel with Aitken relaxation is also proven to work well for strongly coupled problems, is the convergence in this case faster or slower? See (Degroote et al., 2010) for different definitions of coupling algorithms.

It was shown that the experiment discussed in Chapter 5 had problems due to the fine mesh resolution needed to resolve the turbulence. A more detailed research can be done on the mesh convergence for the fluid. Also different turbulence modelling approaches can be better investigated. It would also be beneficial to investigate the memory usage of the solver and improve the efficiency of the parallelization to decrease computational costs and memory usage. When this is achieved the industrial case found in Chapter 5 can be solved with fluid and structured coupled using the IQN-ILS method.

7.2 Possible other test cases

Next to the cases allready used for the current study, there are many other interesting cases that can be used. This section gives a few suggestions and explains why the cases are useful.

Two simple fuel assemblies
In (Liu, 2013) the fluid-structure interaction of two simple fuel assemblies of a PWR are solved numerically, see figure 7.1. The FSI is simulated by the explicit partitioned scheme, in which the flow and structure solvers exchange the data within one time step to implement their coupling for FSI. The flow solver is the commercial CFD software Fluent and the structure solver is an in-house developed beam solver. The effects of dimensionless flow velocity and the number of cylinders on the dynamics of the fuel assemblies are investigated in detail. For small dimensionless flow velocity, the strong vibration is damped into a weak oscillation induced by turbulence. If the dimensionless flow velocity is large enough, the buckling instability occurs. Increasing the number of cylinders in the fuel assembly promotes the occurrence of buckling instability. When the deformations become big the gap between the cylinders may be very small and the cylinders may even touch each other. Thus the computational cells between two cylinders may be squeezed and distorted extremely, leading to the failure of the simulation for flutter instability. This needs improvement of simulation schemes to overcome the difficulty when large deformation of the mesh arises.

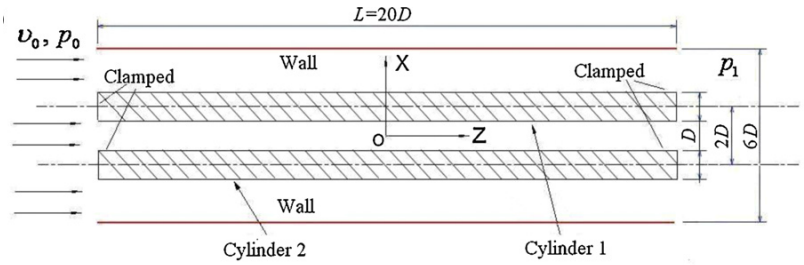

Figure 7.1: Schematic drawing of a simple fuel assembly (Liu, 2013).

This case can be used for:

- Making a step towards more complex geometry
- Checking the difference between the use of a single tube or a tube bundle

Modal characteristics of a flexible cylinder in water flow
Solid brass cylinder in water flow compared to experimental values from (Chen and Wambsganss, 1972) and numerical solution from (De Ridder and Degroote, 2013). In the experiment a solid brass cylinder and a hollow steel cylinder in axial annular water flow, see figure 7.2, are excited harmonically and the resulting vibration characteristics were then determined.

This case can be used for:

- Testing URANS
- Testing quasi newton coupling methods
- Testing a more complex geometry in heavy fluid

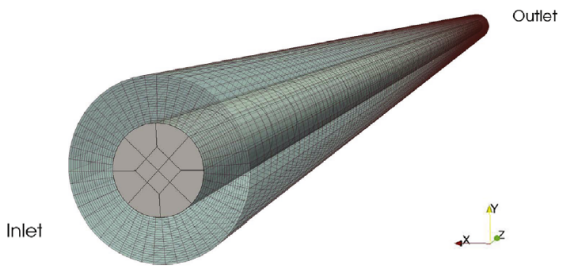

Figure 7.2: Geometry and computational mesh of a cylinder in water flow (De Ridder and Degroote, 2013).

Fluid-elastic instability

Here the onset of fluid elastic instability and the coupling of multiple tubes is simulated, see Figure 7.3. This case was first tested experimentally in (Weaver and Abd-Rabbo, 1985). At a STARCCM conference in 2013 it was shown that this case was also validated using STARCCM+ software coupled with an ANSYS structures solver (STARCCM, 2013).

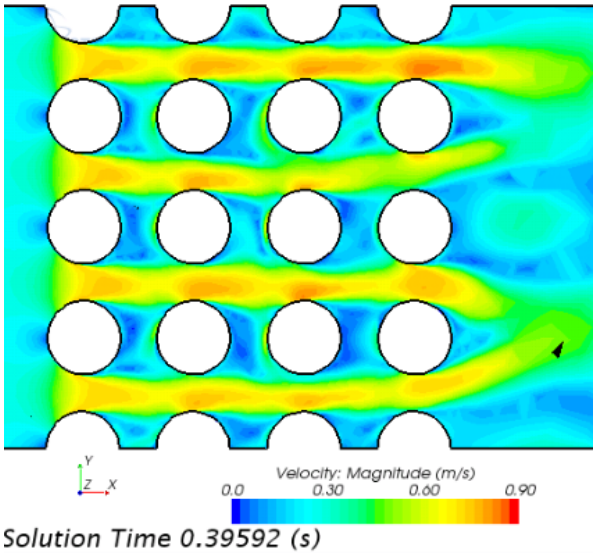

Figure 7.3: Fluid Flow over Flexible Rods (STARCCM+/Abaqus) (STARCCM, 2013)

This case can be used for:

- Testing onset of fluid-elastic instability in a complex tube bundle geometry
- Testing intertube coupling
- Comparing with results from STARCCM gives some confidence in OpenFOAM compared to STARCCM

Bibliography

J.W. Banksa, W.D. Henshawb, and D.W. Schwendeman. An analysis of a new stable partitioned algorithm for fsi problems. part i: Incompressible flow and elastic solids. *Journal of Computational Physics*, 2014.

H. Bijl. Course reader fluid structure interaction(wb1417). An introduction to numerical coupled simulation, 2008.

P. Causin. Added-mass effect in the design of partitioned algorithms for fluid-structure problems. *Computer methods in applied mechanics and engineering*, 2005.

S. Chen. Flow-induced vibration of circular cycylinder structures. *Argonne national laboratory*, 1985.

S.S. Chen and M.W. Wambsganss. Parallel-flow-induced vibration of fuel rods. *Nuclear Engineering and Design*, 1972.

A. de Oliveira Samel Moraes, P. Laranjeira da Cunha Lage, G. Coelho Cunha, and L. Fernando Lopes Rodrigues da Silva. Analysis of the non-orthogonality correction of finite volume discretization on unstructured meshes. In *COBEM*, 2013.

J. De Ridder and J. Degroote. Modal characteristics of a flexible cylinder in turbulent axial flow. *Journal of Fluids and Structures*, 2013.

A. Degroote. Partitioned simulation of fluid-structure interaction. *Arch Comput Methods Eng*, 20:185–238, 2013.

J. Degroote, K.J. Bathe, and J. Vierendeels. Performance of a new partitioned procedure versus a monolithic procedure in fluidstructure interaction. *Computers and Structures*, 87: 793801, 2009.

J. Degroote, A. Souto-Iglesias, W. Van Paepegem, S. Annerel, P. Bruggeman, and J. Vierendeels. Partitioned simulation of the interaction between an elastic structure and free surface flow. *Computer Methods in Applied Mechanics and Engineering*, 2010.

N.J. Georgiadis, D.P. Rizzatta, and C. Fureby. Large-eddy simulation: current capabilities, recommended practices, and future research. *AIAA Journal*, 2010.

E. ter Hofstede and A. H. van Shams, A.and Zuilen. Numerical prepredict of flow induced vibrations in nuclear reactor applications. *NURETH conference*, 2015.

IAEA. URL http://www.iaea.org/About/Policy/GC/GC51/GC51InfDocuments/English/gc51inf-3-att7_en.pdf. Accessed February 2015.

IAEA. *Nuclear Power Reactors in the World*. Number 9789201323101 in 2. IAEA, 2012.

R. I. Issa. Solution of the implicitly discretised fluid flow equations by operator-splitting. *Journal of Computational Physics*, 1986.

U. Kuttler and Wall W. Fixed-point fuid-structure interaction solvers with dynamic relaxation. *Computational Mechanics*, 2008.

M.J. Lighthill. Note on the swimming of slender fish. *Journal of Fluid Mechanics*, 1960.

F. Lindner, M. Mehl, Scheufele K., and Uekermann B. A comparison of various quasi-newton schemes for partitioned fluid-structure interaction. *Coupled Problems*, 2015.

Z.G. Liu. Numerical simulation of the fluidstructure interaction for two simple fuel assemblies. *Nuclear Engineering and Design*, 2013.

K.H. Luk. Pressurized-water reactor internals aging degradation study. Technical report, Oak Ridge National Laboratory, 1993.

OpenFOAM. *User guide, Version 2.2.0*. OpenFOAM Foundation, 2013.

M.P. Paidoussis. Real-life experiences with flow-induced vibration. *Journal of Fluids and Structures*, 2006.

M.J. Pettigrew. Flow-induced vibration: recent findings and open questions. *Nuclear Engineering and Design*, 185:249–276, 1998.

S. Rajesekaran. *Structural Dynamics of Earthquake Engineering: Theory and Application Using MATHEMATICA and MATLAB*. Woodhead Publishing, 2009.

C.M. Rhie and W.L. Chow. A numerical study of the turbulent flow past an isolated airfoil with trailing edge separation. *AIAA J.*, 1983.

B. Simth, B. Bjorstad, and W. Gropp. *Domain decomposition*. Cambridge University Press, 1996.

A.K. Slone, C. Bailey, and M. Cross. Dynamic solid mechanics using finite volume methods. *Applied Mathematical Modelling*, 2003.

STARCCM. The validation of fluid-elastic instabilities in a flexible rod bundle using star-ccm coupled to abaqus, 2013. URL http://www.cd-adapco.com/conference_video/validation-fluid-elastic-instabilities-flexible-rod-bundle-using-star-ccm-coupled.

K. Thulukkanam. *Heat Exchanger Design Handbook, Second Edition*. CRC Press, 2000.

S. Turek. Proposal for numerical benchmarking of fluid-structure interaction between an elastic object and laminar incompressible flow. *Springer Links*, 2006.

A. W. Vreman. An eddy-viscosity subgrid-scale model for turbulent shear flow: Algebraic theory and applications. *Physics of Fluids*, 2004.

Vu and Thi Thank Truc. Testing and optimization of unicorn fluid-structure interaction solver for simulating an industrial problem. Master's thesis, KTH Computer Science and Communication, 2014.

D.S. Weaver. Flow-induced vibrations in power and process plant components progress and prospects. *Journal of Pressure Vessel Technology*, 2000.

D.S. Weaver and A. Abd-Rabbo. A flow visualization study of a square array of tubes in water crossflow. *Journal of Fluids Engineering*, 1985.

Wikimedia. Nuclear power plant, 2014. URL http://upload.wikimedia.org/wikipedia/commons/7/7a/Nuclear_power_plant_pwr_diagram_de.png.

J. Yang. A strongly coupled, embedded-boundary method for fluid structure interactions of elastically mounted rigid bodies. *Journal of Fluids and Structures*, 2008.